# Experimental study of surface wave effects on a horizontal axis tidal turbine: loads and wake dynamics investigation

Marc-Amaury Dufour, Benoît Gaurier, Grégory Germain, Grégory Pinon

Journal of Ocean Engineering and Marine Energy
https://doi.org/10.1007/s40722-026-00476-3

RESEARCH

# Experimental study of surface wave effects on a horizontal axis tidal turbine: loads and wake dynamics investigation

**Marc-Amaury Dufour[1,2] · Benoît Gaurier[2] · Grégory Germain[2] · Grégory Pinon[1]**

Received: 25 September 2025 / Accepted: 27 January 2026


**Abstract**
Surface waves significantly influence the hydro-mechanical response of tidal turbines by inducing variations in structural loading and wake dynamics. Yet, there are few comprehensive databases available for studying these physical processes. To address this gap, we carried out experimental trials on a three-bladed horizontal-axis tidal turbine in a combined wave-current flume tank, testing two wave propagation directions. Our results do not highlight any specific influence related to the direction of wave propagation. It is however shown that waves amplify load fluctuations, particularly at twice the wave frequency, when excited by sidebands of the rotation frequency. Wave-induced variations in wake width appears primarily driven by local flow perturbations due to wave orbital velocity surrounding the wake, whereas wake centroid motion is governed by the wave-generated time-varying dynamics of the rotor. The study of the frequency content of the flow reveals wave-related sidebands around both three and six times the rotational frequency. Frequency analysis of the flow reveals wave-related sidebands around both the blades passing frequency and its second harmonic. This observation is interpreted as wave-induced modulation of tip vortex positions, analogous to waves propagating along a slinky helical spring, which is confirmed by the results of an analytical tip vortices model.

**Keywords** Horizontal axis tidal turbine · Waves · Loads fluctuations · Wake

## 1 Introduction

Tidal stream energy is at the dawn of its development with the first pre-commercial turbine arrays to be deployed soon. Tidal stream energy field sparked interest owing to substantial resources available in specific costal areas. Across Western Europe, the most interesting regions are Northern Scotland, Irish Sea and English Channel (Robins et al. 2015). However, turbines lifespan uncertainties hinder their industrial scale deployment. To tackle this issue, a better assessment of turbines response to velocity fluctuations over their lifetime is required. The scope of the present paper is restricted to horizontal axis tidal turbines (HATT) inasmuch as they are the most common devices.

Two main sources of velocity fluctuations are present in the marine environment: turbulence and surface waves orbital velocities. Turbulence-related influence on HATT is an active field of research. The experimental work of Blackmore et al. (2016) showed the importance of averaging inflow velocity over the rotor swept area to accurately assess the turbine performance while Mycek et al. (2014) evidenced HATT wake shortening with increasing turbulence intensity. Numerical works mainly focused on assessing the blade loads cycles due to different turbulence conditions (Ouro and Stoesser 2019; Mullings and Stallard 2022).

On the other hand, surface waves orbital velocities influence on HATT have primarily been studied through loads variations. Pioneering studies emerged in the late 2000 decade. Barltrop et al. (2006, 2007) compared numerical and experimental results to evaluate waves influence on loads

✉ Grégory Pinon
gregory.pinon@univ-lehavre.fr

Marc-Amaury Dufour
marc-amaury.dufour@univ-lehavre.fr

Benoît Gaurier
benoit.gaurier@ifremer.fr

Grégory Germain
gregory.germain@ifremer.fr

[1] Laboratoire Ondes et Milieux Complexes (LOMC), Normandie Univ, UNIHAVRE, CNRS, 76600 Le Havre, France

[2] Laboratoire d'Hydrodynamique Marine (LHyMar), IFREMER, Centre Manche Mer du Nord, 62200 Boulogne-sur-Mer, France

Published online: 06 March 2026

fluctuations. Their numerical results were obtained using an unsteady blade element momentum theory (BEMT) code modified with a Stokes first order wave model. Subsequent works encompass various approaches. Multiple experimental studies concluded that surface waves do not introduce average performance changes and reported loads fluctuations levels that depended on the tested conditions (Gaurier et al. 2013, 2020; Lust et al. 2013; Luznik et al. 2013). Some studies combining experimental results and modified BEMT focused on the dynamic stall contribution to loads fluctuations under cyclic velocity perturbations (Milne et al. 2013a; Galloway et al. 2014; Scarlett et al. 2019; Perez et al. 2022). The four studies concur: dynamic stall is negligible for turbine reduced velocities ranging from optimum performance to over-speed regions. On the contrary, dynamic stall must contribute significantly to wave-induced loads fluctuations for low reduced velocities when HATT operates in stall regime. Some other studies comparing experimental results and modified BEMT centred the influence of added mass in wave-induced fluctuating loads (Faudot and Dahlhaug 2012; Guo et al. 2018). Both works concluded on the very limited added mass contribution to loads fluctuations. Recently, blade-resolved Eulerian computational fluid dynamics (CFD) techniques have been applied to HATT in wave-current conditions (Tatum et al. 2016; Lloyd et al. 2021; Liu and Park 2023). These studies confirm the previously mentioned conclusions reached with lower fidelity models, namely: no change in average performance and a drastic increase of loads fluctuations. While Lloyd et al. (2021) and Liu and Park (2023) indicated that the free surface motion and loads fluctuations are in phase, Tatum et al. (2016) revealed that HATT loads response experiences a lag phase shift for the highest wave frequencies investigated. Furthermore, in-depth studies also quantified surface waves effect on blade root loads (Draycott et al. 2020; Lam et al. 2023; McNaughton et al. 2025) near turbine optimal operating regime. While the first paper (Draycott et al. 2020) introduced the theory of the rotational sampling of waves orbital velocity and evidenced the associated loads spectra, the other two provided evidence confirming this interpretation. HATT wake studies under surface waves lately emerged. Both numerical (Zilic De Arcos et al. 2023; Liu and Park 2024; Ouro et al. 2024) and experimental (Lust et al. 2020) approaches indicate wake modulation and possible tip vortices merging.

From this overview of wave effects on HATT, two potential contributions are considered. First, given the wide range of reported turbine loads fluctuations, finding a generalised scaling property could be beneficial to the tidal energy community. Furthermore, new investigations on loads response in frequency domain for different turbine tip speed ratios are also of interest. Second, the evaluation of the wave-induced modifications of the turbine wake is still at preliminary stage. Hence, it is also of interest to study the evolution of its properties and frequency content. To fill this gap, the present study reports experimental measurements performed on a HATT model immersed in IFREMER wave and current flume tank. Two surface waves defined by their propagation direction are tested. Their amplitude and time period are set via Froude scaling of in-situ tidal stream energy sites conditions (Filipot et al. 2015; Furgerot et al. 2020). The turbine loads are monitored for different tip speed ratios. Moreover, laser Doppler velocimetry (LDV) measurements are performed in the wake. LDV enables frequency domain analysis of the wake thus supplementing the results of Lust et al. (2020) particle image velocimetry study.

Section 2 emphasises on the upstream flow characterization to ensure the accuracy and reproducibility of the results. Turbine loads response is analysed in Sect. 3 and scalings of loads fluctuations are proposed. In addition, potential loads resonances are evidenced in frequency domain by means of Campbell diagrams. Wave-induced wake width and centroid (i.e. position of maximum velocity deficit) variations induced by the waves are studied via phase average analysis of the LDV flow measurements in Sect. 4. Finally, Sect. 5 presents the energy content of the wake via pre-multiplied spectra. An analytical vortex model that accounts for tip vortices modulation is described.

## 2 Test facility and upstream flow characterization

### 2.1 Experimental set-up

The comprehensive database resulting from the measurement campaign is available online from a public SEANOE repository (Dufour et al. 2025). In-depth description of the test facility and data quality metrics is provided as part of the database.

#### 2.1.1 IFREMER wave and current flume tank

IFREMER wave and current flume tank is located in Boulogne-sur-Mer, North of France. This circulating tank offers an 18 m long, 4 m wide and 2 m deep ($h = 2$ m) working section. The experimental set-up is shown in Fig. 1. Position is described using the Cartesian reference frame $(\vec{e}_x, \vec{e}_y, \vec{e}_z)$ also represented in Fig. 1. The origin is set such that $x = 0$ m corresponds to the turbine model rotation plane, $y = 0$ m is the middle plane of the flume tank and $z = 0$ m is the mean water level. Any position $(\vec{x})$ in the flume tank is expressed as:

$$\vec{x} = x\vec{e}_x + y\vec{e}_y + z\vec{e}_z = (x, y, z). \quad (1)$$

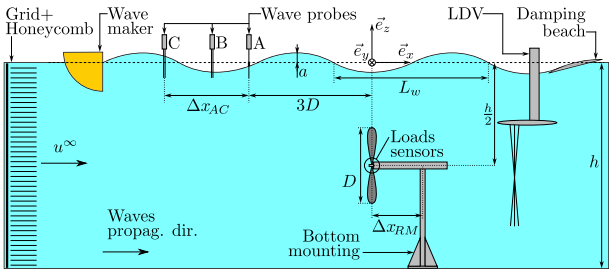


**Fig. 1** Schematic of the experiment in waves following current conditions. Wave maker and damping beach positions are inverted to generate waves opposing current. The dimensions in $x$-direction are not scaled to optimize the schematic layout

Two 250 kW water pumps generate the flow which is loop controlled at a set velocities ($u^\infty$) in the range 0.1 m s$^{-1}$ to 2 m s$^{-1}$. The flow is regularized at the inlet of the working section using flow straighteners: grid and honeycomb. Surface waves are generated using an eight-paddled wave maker, represented in yellow in Fig. 1. A damping beach located on the opposite side of the working section absorbs around 90% of incident waves (Gaurier et al. 2013). Data acquisition is launched when converged conditions are met, meaning waves plus reflection. This process avoids possible change of conditions during the trial. Figure 1 configuration corresponds to the generation of waves following current. By inverting the positions of the damping beach and the wave maker, waves opposing current can also be generated. As a consequence, the presence in the water column of either the wave maker or the damping beach, generates turbulent conditions as well as sheared velocity profiles that are both different from the inlet ones. Those elements are detailed in Sect. 2.2.3.

### 2.1.2 Turbine model and loads sensors

The studied HATT is a 3-bladed scaled model as shown in Fig. 2a. The turbine model is loop-controlled to maintain a preset angular velocity ($\omega_{\text{rot}}$). The blade length ($L_b$) plus the hub radius ($R_h$) constitute half its rotor diameter ($D/2 = L_b + R_h = R$). The blade geometry, known as the IFREMER-LOMC model, was first described by Mycek et al. (2014). However, blades and nacelle have been lately resized and mounted with a new pitch angle. This updated configuration with chord ($c$) and pitch plus twist angle distributions are available in Dufour et al. (2024a) paper. Its rotation centre position ($\vec{x}_{\text{rot}} = (x_{\text{rot}}, y_{\text{rot}}, z_{\text{rot}})$) is immersed at half the water depth. This means that $x_{\text{rot}} = y_{\text{rot}} = 0$ m and that immersion depth is $z_{\text{rot}} = -1$ m. An estimate (as not accounting for the velocity induction) of the chord-based Reynolds number (Re) is:

$$\text{Re} = \frac{c}{\nu}\sqrt{(u^\infty)^2 + r^2\omega_{\text{rot}}^2}, \tag{2}$$

with $c$ the chord, $r$ the corresponding radius, and the fresh water kinematic viscosity $\nu \simeq 1.0 \times 10^{-6}$ m$^2$ s$^{-1}$. Near the optimal operating point, that is to say for $\omega_{\text{rot}} = 8.0$ rad s$^{-1}$, the Reynolds value ranges from $5.5 \times 10^4$ at the blade root, up to $1.3 \times 10^5$ at the tip. In the region contributing most to rotor loads, near 70% of the blade, the Reynolds number equates to $1.2 \times 10^5$. Following the results of Slama et al. (2021), such Reynolds value approaches converged performance of the rotor model. However, slight performance changes in unsteady conditions may occur due to the transition range proximity. The numerical values of those properties are summarized in Table 1. The blockage coefficient is the ratio between the rotor disc area and the flume tank cross section. The obtained blockage value equals 5.1% which is considered small enough not to consider a blockage correction as proposed by Bahaj et al. (2007).

The turbine model is equipped with multiple loads sensors from Sixaxes manufacturer. The shaft is instrumented with a torque ($Q$) and thrust ($T$) transducer which, in particular, measures the rotor thrust without the mounting influence. According to manufacturer datasheet, the respective calibration uncertainties are $\pm 0.1$ N m and $\pm 2.5$ N, representing less than $\pm 1.5$% and $\pm 2.2$% of average values at the turbine optimal operating regime. In addition, 5-component strain gauges equip each of the three blade roots. Signals are collected back to the nacelle via a slip ring. Let $i \in [\![1, 3]\!]$ be the number of each blade. The five components are two

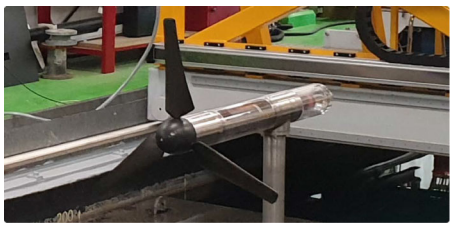

(a) 3-bladed turbine model fixed on its bottom mounting, out of water.

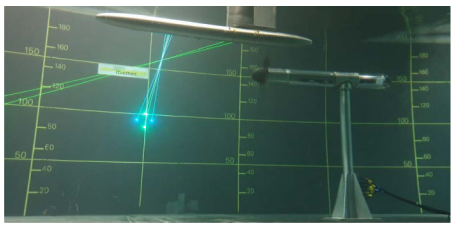

(b) Flow measurement upstream of turbine showing laser Doppler velocimetry beams crossing point.

**Fig. 2** Turbine model and flow measurement during the experiment

**Table 1** Turbine model properties

| Property | Value |
|---|---|
| $D$ [m] | 0.724 |
| $L_b$ [m] | 0.304 |
| $R_h$ [m] | 0.058 |
| Pitch [°] | 4.87 |
| Geometry | IFREMER-LOMC |
| $\vec{e}_x$ rot. dir | Clockwise |
| $z_{\text{rot}}$ [m] | −1.0 |
| Re [–] | $5.8 \times 10^5$ |

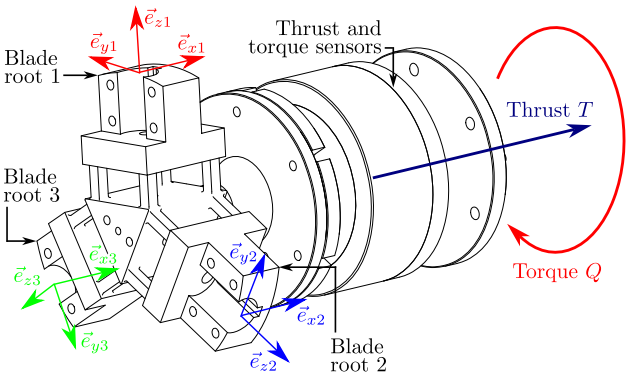


**Fig. 3** Description and coordinate systems of shaft and blade root loads sensors

forces: axial ($f_{x,i}$) and tangential ($f_{y,i}$), together with the three moments: in-plane bending ($M_{x,i}$), out-of-plane bending ($M_{y,i}$) and torsion ($M_{z,i}$). The calibration uncertainty associated with blade root forces is ±1 N whilst it is ±0.2 N m for blade root moments. Sensors locations and coordinate systems are gathered in Fig. 3, presenting a schematic view of the turbine model hub with shaft and blade roots. Loads measurements are sampled at 128 Hz.

### 2.1.3 Flow and free surface measurement techniques

The local flow velocity vector ($\vec{u}(\vec{x}, t)$), function of position and time ($t$), is acquired using a three-component laser Doppler velocimetry (LDV) device from Dantec Dynamics manufacturer. It is represented in Fig. 1 and shown during experiment in Fig. 2b . The three-component LDV relies on three pairs of laser beams. Each pair is of a given colour (i.e. wavelength) and dedicated to a velocity component. All laser beams focus in a small volume of measurement of approximately 0.01 mm$^3$. A regular calibration process of this crossing point ensures an uncertainty below ±0.01 m s$^{-1}$. For the LDV to be working, 10 µm silver-coated glass particles are homogeneously spread in the water volume. Furthermore, the LDV device is used in non-coincident mode which means that velocity is acquired each time a particle is detected. Hence, it is very likely to obtain different acquisition times and frequency rates between the three velocity components. This is the reason why a resampling of all the velocity components on the same time basis is applied as data pre-processing. The obtained sampling frequency of the LDV signals is at least 60 Hz. Given the set velocity, this sampling frequency resolves turbulence scales up to 1 cm or lower. This order of magnitude corresponds to the Taylor length scale values obtained for such flow conditions (Blackmore et al. 2016; Slama et al. 2021; Dufour et al. 2022). As the Taylor length scale characterizes the end of turbulence inertial range (Tennekes and Lumley 1972), this sampling frequency appears well-suited to resolve small scale turbulent fluctuations in the flow. The measured velocity is defined as:

$$\vec{u}(\vec{x}, t) = u_x(\vec{x}, t)\vec{e}_x + u_y(\vec{x}, t)\vec{e}_y + u_z(\vec{x}, t)\vec{e}_z. \quad (3)$$

The free surface of the flow is monitored using three wave probes. Wave probes locations and names are shown in Fig. 1. Wave probe A is located three diameters upstream of the rotor position. The spacing between probes A and C is defined by $\Delta x_{AC} = 1.21$ m. This distance approximately corresponds to $1.7D$. Wave probes signals are recorded at 128 Hz and synchronised with turbine measurements. Two types of wave probes are used in the experiment. Wave probes B and C are resistive. They consist in two metal rods. The variation of their immersion depth changes the associated dipole resistance. A regular calibration process linearly links the measured voltage with the water elevation. It enables to maintain the uncertainty around ±5 mm. Those resistive probes are considered to accurately track the instantaneous phase of the surface waves motion. Hence, the reference phase signal for surface wave motion is probe B. Wave probe A is of dynamic type from Kenek manufacturer. The datasheet provides an uncertainty of ±2 mm on free surface elevation measurement. It works using an highly responsive servo motor positioning a lightweight pre-calibrated electrode needle at the free surface level. The needle position then tracks the free surface motion.

### 2.1.4 Combined standard uncertainty of sensors

The combined standard uncertainties associated to each sensor is assessed following Bell (2001) by aggregating multiple uncertainty sources: calibration (mentioned above in sensor description), acquisition system resolution, temporal convergence and acquisition repeatability. The obtained values, detailed in Table 2, confirm the relevance of the experimental set-up and demonstrate the level of confidence in the measurements analyzed in this work. The database manual (Dufour et al. 2025) details the uncertainty analysis process.

**Table 2** Combined standard uncertainties

| Measured quantity | Value of the combined standard uncertainty |
|---|---|
| Blade root forces | 3.2 N |
| Blade root moments | 0.32 N m |
| Shaft torque | 0.25 N m |
| Rotor thrust | 3.0 N |
| Resistive wave probes | 8.2 mm |
| Flow velocity from LDV | 0.033 m $s^{-1}$ |

## 2.2 Flow and surface waves characteristics

### 2.2.1 Froude scaling and conditions definition

Let Fr be the Froude number defined by:

$$\mathrm{Fr} = \frac{u^\infty}{\sqrt{gh}}, \tag{4}$$

with $g$ the gravitational acceleration. Keeping this number constant between two geometrically-scaled situations guarantees that the gravity effects consequences are physically well-reproduced. This process is known as Froude similarity. It is, for instance, detailed by Molin (2023). Let $\Lambda$ be the geometry scale on lengths between the real scale and the flume tank scale. Hence, real scale water depth ($H$) verifies:

$$H = \Lambda h. \tag{5}$$

In candidate sites for tidal farms deployment, the water depth is about $H = 40$ m (Robins et al. 2015; Guillou et al. 2016; Moreau et al. 2022). With a flume tank water depth being $h = 2$ m, the scale factor yields: $\Lambda = 20$ (Eq. (5)). In the present experiment, the set velocity is $u^\infty = 0.8$ m $s^{-1}$, giving a Froude number of Fr $\simeq 0.18$. The real-scale current velocity respecting Froude similarity is defined by: $u^\infty\sqrt{\Lambda}$. It is obtained by injecting Eq. (5) into Eq. (4). Hence, the real-scale current velocity value associated to the present experiment is: $u^\infty\sqrt{\Lambda} \simeq 3.6$ m $s^{-1}$. This real-scale velocity is consistent with reported peak velocities at tidal stream energy sites (Robins et al. 2015; Furgerot et al. 2020). The set velocity of the experiment is a compromise between the constraints of being high enough so that the turbine behaviour approaches Reynolds independence (Slama et al. 2021) and, at the same time, small enough to respect Froude similarity. Scaling the experiment using the Froude similarity is justified as the main goal is the accurate assessment of the surface wave effects on the turbine.

Experimental wave cases are defined following real-scale wave conditions encountered at tidal stream energy sites. Most common sea states, meaning significant wave height ($H_S$) and peak period ($T_P$), are reviewed from sites along the English Channel. These conditions are: Paimpol–Bréhat of $H_S \simeq 0.8$ m and $T_P \simeq 9$ s (Filipot et al. 2015; Moreau et al. 2022), Fromveur Strait of $H_S \simeq 1$ m and $T_P \simeq 10$ s (Guillou et al. 2016) and Alderney Race of $H_S \simeq 1$ m and $T_P \simeq 8$ s (Furgerot et al. 2020). Consequently, a significant wave height of $H_S = 2$ m and a peak period of $T_P = 10$ s are chosen because they correspond to conditions that exceed the representative sea states at all those tidal stream energy sites. Applying Froude similarity provides the definition of the wave desired properties:

$$H_S = \Lambda 2a^\infty, \quad \text{and} \quad T_P = T_w^\infty\sqrt{\Lambda}, \tag{6}$$

with $a^\infty$ being the desired wave amplitude in the flume tank, which is half the wave crest-to-trough, and $T_w^\infty$ being the reference wave period in the flume tank. Using formulae of Eq. (6), one easily obtains the desired wave amplitude: $a_\infty \simeq 0.05$ m and set frequency: $1/T_w^\infty = 0.45$ Hz. Eventually, the wave propagation direction is considered. Using a seven-year numerical hindcast, Lewis et al. (2014) evidenced that inline surface waves conditions occur from 10% to 50% of the time depending on the tidal stream energy site. Even though those conditions are not the most common ones, they are expected to be the most detrimental ones when considering turbines unsteady hydrodynamic loadings. This is the reason why the present study focuses on such inline wave conditions. Two wave cases are then considered, both aiming at $a_\infty \simeq 0.05$ m and $1/T_w^\infty = 0.45$ Hz. One wave case propagates following the current direction ($\vec{e}_x$, Fig. 1), denoted "FO" in the rest of the paper. The second one propagates against, or opposing, the current direction, hence denoted "OP".

### 2.2.2 Surface waves characterization

The surface waves frequency ($f_w = 1/T_w$) in the experiment is slightly different from the reference given above ($1/T_w^\infty$) due to wave maker transfer function as explained in Appendix B.1. This justifies the change in notation as using exact $f_w$ value is of prime importance for the signal processing tools. As the wave maker is loop controlled at the exact $f_w$ value, no frequency shift is observed during the experiment. The wave maker controller produces first order monochromatic waves in the present experiment. Let $\eta$ be the free surface elevation. The wave probes measurements are defined as: $\eta_Y(t)$ with $Y \in \{A, B, C\}$. The free surface signals are filtered at the wave frequency ($f_w$) using in-house second order band pass filters (Tisserand et al. 2009; Legrand 2013) of narrow width with a $Q$ factor value of 8. This filtering operation is denoted $\tilde{\bullet}$. Hence, the filtered free surface elevation is first order and monochromatic such that:

$$\tilde{\eta}_Y(t) = a_Y \sin(\omega_w t + \varphi_Y), \tag{7}$$

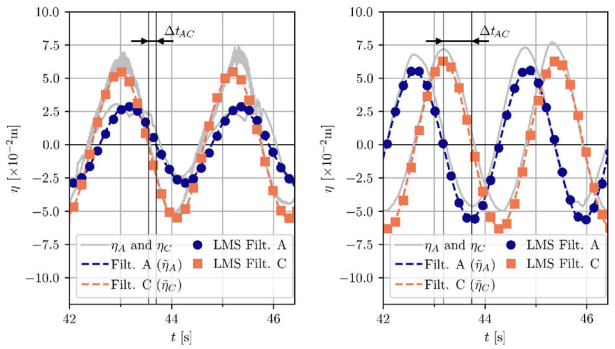


(a) Following (FO) wave case. (b) Opposing (OP) wave case.

**Fig. 4** Time series snippets of wave probes A and C measurements (grey lines). The band-pass-filtered signals (dashed lines) and reconstructions using LMS-obtained parameters (markers) are superimposed (color figure online)

with $\omega_w = 2\pi f_w$ the waves angular frequency and $\varphi_Y$ the phase associated to each probe position. Surface waves amplitude ($a_Y$) and phase ($\varphi_Y$) at the measurement position are evaluated with an in-house sine least mean square (LMS) at known frequency ($f_w$) algorithm. LMS implementation details are provided by Jacquelin (2014). To evaluate the relevance of this process, representative snippets of probes A and C time series are shown in Fig. 4. The probes measurements (grey) are superimposed with processed results for probes A (blue) and C (orange). A good agreement is observed between the direct probes measurements, the filtered free surface elevation (left member of Eq. (7), dashed lines) and the reconstruction using LMS-evaluated parameters (right member of Eq. (7), markers). It confirms that, in the experiment, surface waves are very close to being monochromatic and first order. Consequently, the presented signal processing appears suitable. This assumption not only enables to clearly define wave properties but it is also used afterwards to perform phase averaging with respect to waves motion. A question is raised by the amplitude difference between probes A and C in the FO wave case (Fig. 4a). This phenomenon is generated by the flume tank response to long wavelengths. In such conditions, the flume tank is prone to experience a partial standing wave which spatially alters the amplitude of propagating waves (Méhauté 1976). It highlights the need for monitoring the wave amplitude at different locations, in particular for FO wave cases, to obtain a better accuracy via spatial averaging.

The wavelength ($L_w$), and associated wave number ($k_w = 2\pi/L_w$), are assessed using the signals from the two most distanced wave probes (A and C). The wavelength is defined by applying the phase velocity definition:

$$L_w = \frac{\Delta x_{AC}}{\Delta t_{AC}} T_w, \tag{8}$$

with $\Delta x_{AC}$ the distance between probes A and C along $\vec{e}_x$, and $\Delta t_{AC}$ the time delay between the two probes signals as shown in Fig. 4. The time delay ($\Delta t_{AC}$) is obtained from the phase difference between the two LMS results ($\Delta\varphi_{AC}$). The inter-probes spacing is inferior to half the wavelength for both wave cases. Knowing this leads to the phase difference definition used in Eq. (9). The time delay is then obtained as:

$$\Delta t_{AC} = \frac{\Delta\varphi_{AC}}{\omega_w} \quad \text{with}$$
$$\Delta\varphi_{AC} = \begin{cases} |\varphi_A - \varphi_C| & \text{if } |\varphi_A - \varphi_C| \leq \pi, \\ 2\pi - |\varphi_A - \varphi_C| & \text{otherwise.} \end{cases} \tag{9}$$

Resulting wave properties are gathered in Table 3. And some supplements regarding frequency and wavelength are available in Appendix B.1. As numerous acquisitions are available from the dataset, surface wave properties reported in Table 3 are median values over 40 acquisitions of four minutes each. Following the data curation explained above, the amplitude ($a$) is the average of each probe median. The associated wave steepness ($k_w a$) is also reported. The steepness small values confirm the validity of using the first order waves assumption. The wave classification by Méhauté (1976) with respect to water depth using $h/L_w$ criterion is also specified in Table 3. Overall, according to the values reported in Table 3, the wave conditions in the experiment match well the Froude scaling requirements. Hence, the present study conclusions upon wave effects on turbine must be applicable to real scale devices. Finally, the work of Linton (1988) on two-dimensional submerged vertical plates evidences that the wave reflection by the turbine cannot exceed a few percent for the considered wave numbers (Table 3) at this immersion depth. It is then negligible compared to the wave reflection generated by the damping beach and it is not further considered.

### 2.2.3 Upstream flow characterization

Although the free surface characterization is important to relate the experimental conditions to in-situ sea states, the crucial aspect lies in the assessment of the inflow conditions. The velocity vector is described using the Reynolds decomposition supplemented with a periodic component following (Hussain and Reynolds 1970):

$$\vec{u}(\vec{x}_c, t) = \overline{\vec{u}}(\vec{x}_c) + \underbrace{\vec{u}^w(\vec{x}_c, t)}_{=\vec{u}^d(\vec{x}_c,t)} + \vec{u}'(\vec{x}_c, t), \tag{10}$$

with a time-averaged component ($\overline{\vec{u}}$), the wave orbitals contribution ($\vec{u}^w$) and a turbulent part ($\vec{u}'$). For the sake of explanation, a "dynamic" velocity component ($\vec{u}^d$) containing both wave orbitals and turbulence is defined. Details on

**Table 3** Measured surface waves properties

| Wave case | $f_w$ [Hz] | $L_w$ [m] | $h/L_w$ [–] | Classification | $a$ [m] | $k_w a$ [–] |
|---|---|---|---|---|---|---|
| FO | $\simeq 0.45$ | 15.9 | 0.13 | Intermediate | $4.5 \times 10^{-2}$ | $1.8 \times 10^{-2}$ |
| OP | $\simeq 0.45$ | 4.7 | 0.43 | Intermediate near deep water | $6.3 \times 10^{-2}$ | $8.4 \times 10^{-2}$ |

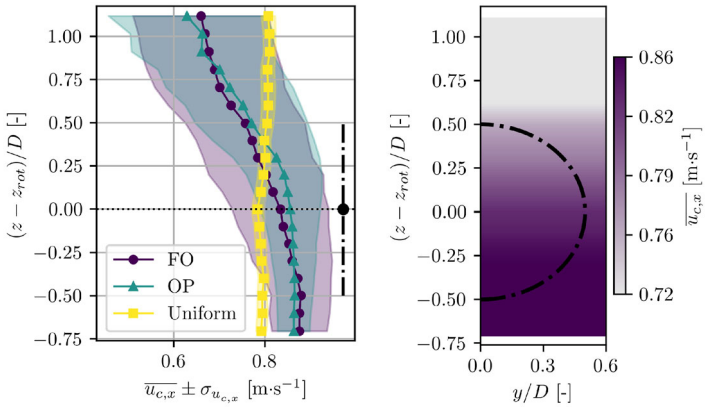


(a) Axial velocity profiles. (b) FO $y$-expanded profile.

**Fig. 5** **a** Vertical characterization profiles of time-averaged axial velocity ($\overline{u_{c,x}}$) for FO, OP and uniform conditions represented with lines and markers. Shaded areas indicate the standard deviation magnitude ($\sigma_{u_{c,x}}$). **b** FO profile expansion on $y$-axis highlights the shear over the rotor swept area

the formalism are available in Appendix A. The flow is characterized along vertical profiles. Hence, the measurement positions ($\vec{x}_c$) vary along the vertical axis ($\vec{e}_z$) with fixed ($x_c$, $y_c$) coordinates. The upstream flow conditions cannot be summarized to the ones at the inlet of the working section (i.e. immediately after the flow straighteners) due to the perturbations introduced by the wave maker (FO) or the damping beach (OP). This is the reason why vertical profiles of the velocity were measured prior to the experiment: without the immersed turbine model and at the mounting position, which is the flume tank reference position. Following Fig. 1, the characterization positions are (in meters):

$$\vec{x}_c = (\Delta x_{RM}, 0, z) \quad \text{with} \quad z \in [-1.9, -0.1] \quad \text{and} \quad \Delta x_{RM} \simeq 0.59. \tag{11}$$

A simplified notation can be derived for the characterization velocity:

$$\vec{u}_c(z, t) = \vec{u}(\vec{x}_c, t). \tag{12}$$

Figure 5 represents the time-averaged $x$-component velocity ($\overline{u_{c,x}}$, Eqs. (10) and (12)) supplemented with the associated standard deviations ($\sigma_{u_{c,x}}$). The velocity standard deviation equates to the purely turbulent standard deviation ($\sigma_{u'_{c,x}}$) for the uniform condition while it corresponds to the dynamic standard deviation ($\sigma_{u^d_{c,x}}$) for wave cases. While Fig. 5a details its variations with depth, Fig. 5b focuses on the shear across the rotor swept area. The rotor is represented with a black dash-dot line and the centreline ($z_{\text{rot}} = -1$ m) is indicated with a black dotted line in Fig. 5a. Vertical profiles for three upstream conditions are shown in Fig. 5a. For the same set velocity ($u^\infty = 0.8$ m s$^{-1}$), the two studied flows with surface waves are represented against the "uniform" condition meaning with no wave maker nor damping beach immersed. Both FO and OP conditions suffer from sheared velocity profiles because of the wave maker or damping beach presence. Those technical constraints in the experiment design could not be avoided. Although such sheared profiles are not representative of frequently encountered conditions in tidal stream energy sites, the relative velocity difference between rotor bottom and tip is consistent with standard marine conditions (Evans et al. 2013; Lewis et al. 2017; Bourgoin et al. 2020).

The shear and high fluctuation levels in both FO and OP velocity profiles raise concerns in correctly defining the upstream velocity (or any exponent) perceived by the rotor, in particular for performance assessment. As a matter of fact, Blackmore et al. (2016) showed that the time average of any velocity exponent ($\overline{u^n_{c,x}}$ for $n \in \mathbb{N}$) should be performed after its exponentiation to obtain accurate turbine performance in highly turbulent environments, echoing a similar observation performed by Tian et al. (2020) in wave only cases. Moreover, as also advised by Blackmore et al. (2016), a disc integration of the time-averaged velocity exponents has to be performed to circumvent the shear influence. The disc average process, denoted $\widehat{\bullet}$, consists in a normalized disc integration which is evaluated here by means of an in-house trapezoidal rule algorithm. It is performed on profiles of time-averaged velocity (or any exponent) that are expanded along $y$-axis, as shown in Fig. 5b for FO conditions. In a word, to account for both time-

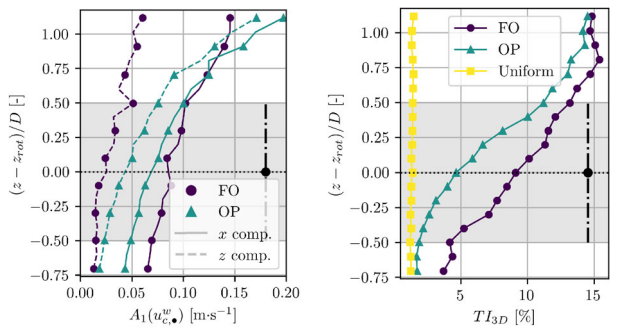


(a) Orbital velocity amplitude. (b) Turbulence intensity.

**Fig. 6** **a** Vertical profiles of orbital velocity amplitudes ($A_1(u^w_{c,\bullet})$) for both spatial components: $\bullet \in \{x, z\}$. **b** Vertical profiles of 3D turbulence intensities ($TI_{3D}$). The significant shear of turbulent fluctuations in FO and OP conditions is evidenced

dependent fluctuations and shear effect in rotor perceived velocity, the disc-averaged velocity of exponent $n \in [\![1, 3]\!]$ is defined as:

$$\widehat{u^n_{c,x}} = \frac{1}{\pi R^2} \iint\limits_{\substack{y,z\in\mathbb{R} \\ y^2+z^2\leq R^2}} \overline{u^n_{c,x}}(z)\, \mathrm{d}y\, \mathrm{d}z. \tag{13}$$

To complete upstream conditions characterization, the dynamic velocity (Eq. (10)), which includes both turbulence and waves, is studied using Figs. 6, 7 and 8. Figure 6 presents the vertical profiles of orbital velocities amplitudes (a) and turbulence intensities (b). Turbine area is highlighted by means of the grey-coloured background. Figure 7 presents axial velocity PSDs computed using Welch (1967) method. Concerning the wave cases, the dynamic PSDs ($S_{u^d_x u^d_x}$) are shown in lightly coloured lines whereas turbulence only PSD spectra ($S_{u'_x u'_x}$) are plotted in plain lines. The characterization subscript ("$c$") is omitted to simplify the PSD notation. Figure 8 presents axial velocity autocorrelations. Similarly, dynamic component autocorrelations ($R(u^d_{c,x})$) are presented in lightly coloured lines while turbulence only autocorrelations ($R(u'_{c,x})$) are shown in plain lines with markers. Figures 7 and 8 come from a single measurement point near turbine immersion depth.

First, the surface waves orbital velocities are quantified over the water column. Orbital velocities amplitudes are obtained by means of the sine least mean square (LMS) method at wave frequency ($f_w$) applied on pre-filtered velocity signals. Details are provided in Appendix A.3. For a given spatial component $\bullet \in \{x, z\}$, the characterization orbital velocity is then:

$$u^w_{c,\bullet}(z, t) = A_1(u^w_{c,\bullet})(z)\ \sin\!\left(\omega_w t + \varphi_1(u^w_{c,\bullet})\right). \tag{14}$$

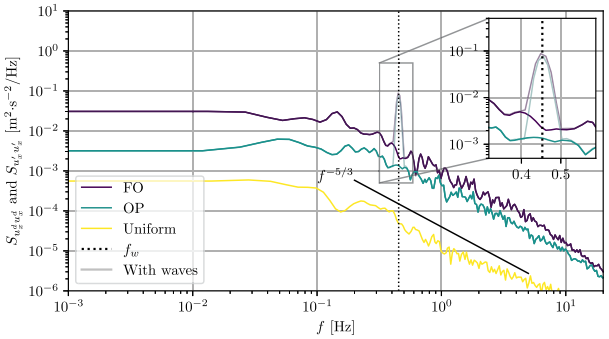


**Fig. 7** Velocity power spectral densities (PSD) from a single measurement point near immersion depth ($z_{\text{rot}} = -1$ m). While plain lines present PSD spectra on turbulent fluctuations ($S_{u'_x u'_x}$), lightly coloured lines present PSD spectra on dynamic velocity ($S_{u^d_x u^d_x}$). Characterization subscript ("$c$") is omitted to simplify the notations

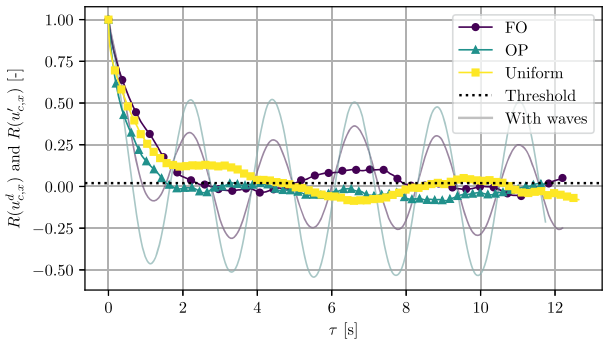


**Fig. 8** Velocity autocorrelations from a single measurement point near immersion depth ($z_{\text{rot}} = -1$ m). While plain lines present autocorrelations on turbulent fluctuations ($R(u'_{c,x})$), lightly coloured lines are dedicated to dynamic velocity ($R(u^d_{c,x})$)

Both $x$ and $z$ components of orbital amplitudes ($A_1(u^w_{c,\bullet})$) are shown in Fig. 6a. The low values of wave steepness (Table 3) indicate that Stokes first order (Airy) wave-current theory is applicable (Méhauté 1976; Rey et al. 2007). This theory states that orbital amplitude profiles of deep water waves are more sheared than the ones of intermediate water depth waves. This is consistent with results presented in Fig. 6a where OP orbital amplitude profiles are more sheared than FO ones. Following the idea proposed by Whelan et al. (2009), Faudot and Dahlhaug (2012) and Milne et al. (2013a), a current number ($\mu^w$) is introduced to quantify the relative flow unsteadiness due to orbitals:

$$\mu^w = \frac{\widehat{A_1(u^w_{c,x})}}{\widehat{u_{c,x}}}. \tag{15}$$

Evaluating this ratio for FO wave case yields 0.11 meaning that, on the rotor swept area, orbitals relative motion is about 11% of reference velocity. For OP wave case, orbitals relative motion is about 8% of reference velocity ($\mu^w \simeq 0.08$). For both cases, waves orbital amplitude are of similar order of

magnitude. Eventually, a remaining question lies in the extent to which the presented method is able to extract completely the wave component from the velocity signal. To verify the absence of wave contribution in the extracted turbulent component, the dynamic and turbulent results of Figs. 7 and 8 are compared. In the spectral domain, the spike at wave frequency ($f_w$) vanishes when the wave component is removed. In the temporal domain, autocorrelation shows that oscillations at wave period ($T_w$) are completely removed when wave component is extracted. Hence, it can be concluded that wave orbital velocities are accurately quantified and that turbulence signal is not disturbed by orbitals.

Finally, the turbulence component ($\vec{u}'_c$, Eqs. (10) and (12)) remains to be studied. Turbulence is described using vertical profiles of turbulence intensity (Fig. 6b ) and supplemented by the aforementioned single-point PSDs and autocorrelations. The three-dimensional turbulence intensity ($TI_{3D}$) is defined as:

$$TI_{3D} = \sqrt{\frac{\sigma^2_{u'_{c,x}} + \sigma^2_{u'_{c,y}} + \sigma^2_{u'_{c,z}}}{3\left(\overline{u_{c,x}}^2 + \overline{u_{c,y}}^2 + \overline{u_{c,z}}^2\right)}}. \tag{16}$$

Figure 6b evidences significantly sheared turbulence intensity profiles. The turbulence intensity increases from bottom to top. This phenomenon is generated by either the wave maker or the damping beach immersion at the inlet. It does not result from wave orbital velocities as they have been extracted from turbulence signals. Hence, the turbine experiences a significant vertical shear of turbulence. While the turbulence intensity ($TI_{3D}$) at the rotor bottom respectively equates to 2% and 4% for OP and FO conditions, it respectively raises up to 11% and 13% at the rotor top. It stresses on the importance of using disc average (denoted $\widehat{\bullet}$, see application on velocity exponents in Eq. (13)) to assess the flow properties faced by the turbine. Hence, disc-averaged turbulence intensity is $\widehat{TI_{3D}} \simeq 9\%$ for FO wave case and $\widehat{TI_{3D}} \simeq 5\%$ for OP wave case. Such sheared profiles are not ideal to best separate the unsteadiness sources effects on the rotor response. However, similar turbulent profiles are reported in marine tidal stream energy sites (Bouferrouk et al. 2016; Furgerot et al. 2020; Bourgoin et al. 2020). Most importantly, disc-averaged turbulence intensities reported here are comparable to marine environment values (Thomson et al. 2012; Milne et al. 2013b; Bouferrouk et al. 2016). Moreover, the velocity PSD spectra (Fig. 7) present a $-5/3$ slope over the inertial range, in logarithmic scale. It shows that the turbulence dissipation cascade follows Kolmogorov's law (Tennekes and Lumley 1972) and is consistent with respect to PSD spectra reported in the literature for similar upstream conditions (Blackmore et al. 2016; Durán Medina et al. 2017; Payne et al. 2018). More in-depth details concerning turbulence nature with Reynolds stress tensor and integral length scale evaluation are available in Appendix B.2.

## 3 Surface wave effects on turbine loads

### 3.1 Performance coefficients average and fluctuations

Following the work of Blackmore et al. (2016), the disc-averaged velocity (Eq. (13)) is used as reference to define the time-averaged tip speed ratio ($\overline{TSR}$), power coefficient ($\overline{C_P}$) and thrust coefficient ($\overline{C_T}$):

$$\begin{aligned}
\overline{TSR} &= \frac{R\,\overline{\omega_{\text{rot}}}}{\widehat{\overline{u_{c,x}}}},\\
\overline{C_P} &= \frac{\overline{\omega_{\text{rot}}\,Q}}{\frac{1}{2}\rho\pi R^2\widehat{\overline{u^3_{c,x}}}},\\
\overline{C_T} &= \frac{\overline{T}}{\frac{1}{2}\rho\pi R^2\widehat{\overline{u^2_{c,x}}}}.
\end{aligned} \tag{17}$$

The fluid density is denoted by $\rho$. The turbine model angular velocity ($\omega_{\text{rot}}$), shaft torque ($Q$) and thrust ($T$) are monitored via the sensors presented in Sect. 2.1.2. Data acquisitions are performed over four-minute runs. This duration is long enough to reach convergence of the studied statistical properties as previously detailed by Mycek et al. (2014) and Blackmore et al. (2016). As the turbine is loop-controlled to maintain a constant angular velocity ($\omega_{\text{rot}}$), the associated standard deviation is less than 1% for all $TSR$ values in all studied conditions. Despite these limited fluctuations, the tip speed ratio is time-averaged as a matter of mathematical consistency. The resulting value nearly equates the reference set value.

Turbine time-averaged performance as function of tip speed ratio are presented in Fig. 9. For each $\overline{TSR}$, the performance standard deviation is highlighted using colour-filled areas. Wave cases results are compared to the reference ones in uniform flow. Average performance remains nearly unaltered by waves presence, be it FO or OP waves. This result is widely confirmed by literature (Lust et al. 2013; Luznik et al. 2013; Gaurier et al. 2013; Guo et al. 2018; Scarlett et al. 2019; McNaughton et al. 2025). Yet, compared to the uniform flow, both wave cases curves predict a slight increase of power extraction ($\overline{C_P}$) in the highest $\overline{TSR}$ (over-speed) region. It is attributed to the stronger flow unsteadiness produced by the immersion of wave-generating devices (wave maker or damping beach). As a matter of fact, high turbulence regimes change energy harvesting mechanisms and may result into slight performance increase (Gambuzza and Ganapathisubramani 2021). However, this slight performance increase is

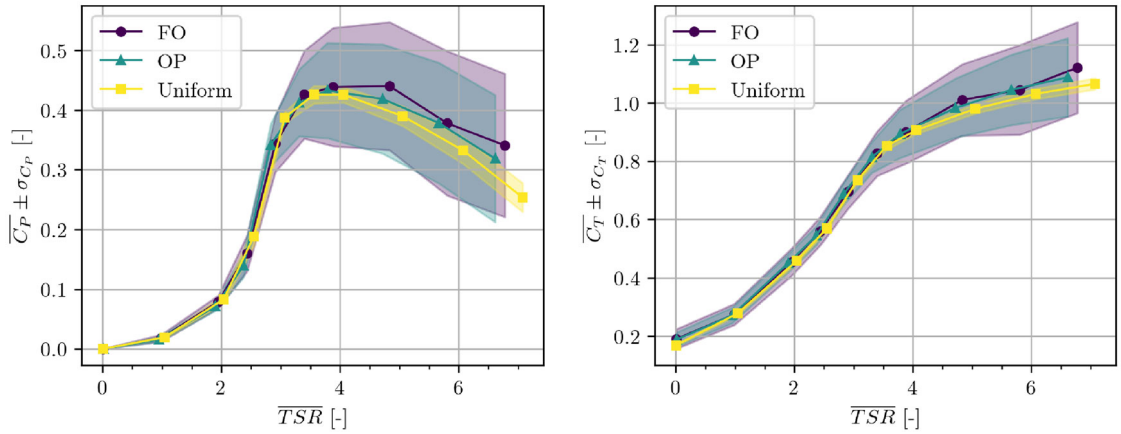


(a) Power coefficient. (b) Thrust coefficient.

**Fig. 9** Averages (lines with markers) and standard deviations (colour-filled areas) of turbine power (**a**) and thrust (**b**) coefficients as functions of time-averaged tip speed ratio. Each inflow case is represented with a dedicated colour

not expected to occur when turbulent conditions are kept constant between with and without wave cases. To illustrate this, a numerical study by Scarlett et al. (2019) on a single full-scale HATT evidenced that a slight decrease of average power coefficient is expected in wave conditions due to flow separation occurring more often on parts of the blades. Figure 9 also highlights that loads standard deviations of both wave cases increase with $\overline{TSR}$. This phenomenon is also reported in multiple studies (Gaurier et al. 2013; Watanabe et al. 2023; McNaughton et al. 2025). It comes from the rotational sampling of inflow velocity fluctuations performed by the blades. This phenomenon is specifically evidenced by Galloway et al. (2014) and Draycott et al. (2020). In the case of wave orbital velocities, velocity fluctuations perceived by the blades significantly increase with the turbine rotation. Hence the loads fluctuations are reduced at low $\overline{TSR}$. In the present study, the power (resp. thrust) standard deviation reaches about 23% (resp. 12%) of average load at optimal $\overline{TSR}$ in FO case. Such orders of magnitude are similar to other studies of comparable wave parameters (Gaurier et al. 2013, 2020; Draycott et al. 2019; Guy et al. 2024).

The question that arises is: to what extent are the loads fluctuations similar from one inflow case to another? Scaling loads fluctuations by the associated averages provides interesting insights on relative variations across $\overline{TSR}$ range (Slama et al. 2021; Watanabe et al. 2023). Nevertheless, it does not enable to cross-compare the results from one case to another nor does it permit to establish a relation that can help evaluate a priori loads fluctuations. To reach this objective, the current number ($\mu^w$, Eq. (15)), introduced by Whelan et al. (2009), Faudot and Dahlhaug (2012) and Milne et al. (2013a), is considered as a scaling number. It quantifies the disc-averaged orbital amplitude with respect to reference current velocity. While the scaling potential of this number appears interesting for turbines facing a well-defined periodic velocity forcing, it lacks generality to enable cross-comparison with turbulent only inflows. Hence, the approach developed separately by Draycott et al. (2019) for waves and Druault et al. (2022) for turbulence is used. It demonstrates that turbines respond linearly to spatially averaged velocity fluctuations. From this approach, it is obtained that the variance of any shaft load ($B$), be it torque ($Q$), power ($P$) or thrust ($T$), is proportional to the time average of the squared instantaneous disc-averaged dynamic velocity. It is reminded here that the dynamic velocity ($u^d_{c,x}$) includes both turbulence ($u'_{c,x}$) and wave orbital ($u^w_{c,x}$) fluctuations (Eq. (10)). It reads:

$$\sigma_B^2 \propto \overline{\widehat{u^d_{c,x}}^2} \quad \text{with } B \in \{Q, P, T\}. \tag{18}$$

However, the time average of the squared disc-averaged dynamic velocity cannot be directly evaluated. To circumvent this constraint, the disc integration (Eq. (13)) is mathematically interpreted as a scalar product to obtain an upper bound using Cauchy–Schwarz inequality:

$$\overline{\widehat{u^d_{c,x}}^2} \leq \overline{\widehat{(u^d_{c,x})^2}}. \tag{19}$$

Fubini's theorem is used to invert the order of the temporal and spatial integrations:

$$\overline{\widehat{(u^d_{c,x})^2}} = \overline{\widehat{(u^d_{c,x})^2}} = \widehat{\sigma^2_{u^d_{c,x}}}. \tag{20}$$

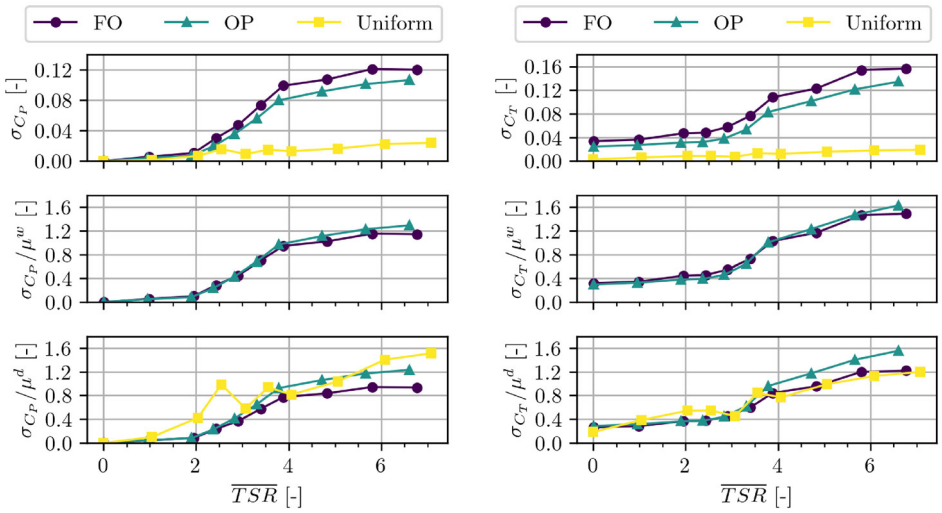


(a) Power coefficient fluctuations.

(b) Thrust coefficient fluctuations.

**Fig. 10** Standard deviations of the performance coefficients as functions of average tip speed ratio (top) for the three studied inflows: FO (dark purple), OP (blue) and uniform (yellow). Two normalization factors based upon velocity fluctuations are tested below: current number (middle) and dynamic number (bottom)

As a result, a normalized number quantifying the dynamic velocity fluctuations is:

$$\mu^d = \frac{\sqrt{\widehat{\sigma^2_{u^d_{c,x}}}}}{\widehat{u_{c,x}}}. \tag{21}$$

For the turbulent only inflow cases, the obtained number is a disc-averaged interpretation of the familiar streamwise, or 1D, turbulence intensity often used in the literature (Roy et al. 2004; Milne et al. 2013b). Standard deviation of the performance coefficients as function of $\overline{TSR}$ is represented in the upper graphs of Fig. 10. In the middle graphs, the standard deviations are normalized by the current number ($\mu^w$, Eq. (15)). In the bottom graphs, the standard deviations are normalized by the dynamic number ($\mu^d$, Eq. (21)). Both wave cases curves superimpose when applying the current number scaling. However, the current number scaling is meaningless without waves, justifying the study of the dynamic number scaling. This scaling raises the fluctuations of the uniform flow up to the same levels as the wave cases. Consequently, standard deviation of the performance coefficients normalized by velocity fluctuations are interpreted as an intrinsic characteristic of a given turbine and could be used to estimate a priori the level of loads fluctuations in a given environment. Focusing on the wave cases, Fig. 10 also evidences that current number ($\mu^w$) scaling better performs than the dynamic number ($\mu^d$) one. This observation can be explained by the HATT response amplitude operator (RAO). As experimentally shown by Gaurier et al. (2022), a turbine RAO can be modelled by a low pass filter with a constant gain at low frequency, up to a cutting frequency between $10^{-1}$ Hz and 1 Hz. This observation is supported by theoretical (Tobin et al. 2015) and experimental (Chamorro et al. 2015; Gambuzza and Ganapathisubramani 2021) studies on horizontal axis wind turbines. As a consequence, the turbine responds linearly to velocity fluctuations only in the low frequency range which includes wave-induced orbital velocities. However, the dynamic number also accounts for turbulent velocity fluctuations, partly high frequency, that are then not perceived by the turbine. This leads to a partially inconsistent scaling using the dynamic number. To summarize, in case of low frequency periodic velocity forcing, a scaling based upon the current number appears better suited.

### 3.2 Loads frequency domain response

Frequency domain analysis completes this study of wave effects on a single HATT. Shaft torque ($Q$) and thrust ($T$) power spectral densities (PSD) are respectively denoted $S_{QQ}$ and $S_{TT}$, and shown in Fig. 11a and b. The PSDs using Welch (1967) algorithm with Hann windowing and loads signals are sliced in segments of $2^{13}$ points that are half-size overlapped. To enable the cross comparison between the different cases, all the PSDs in Fig. 11a, b are assessed for the same time-averaged rotation frequency ($f_{\text{rot}}$), omitting the time average symbol to ease readability. Due to the different inflow conditions, a similar rotation frequency yields a slightly different time-averaged $TSR$, namely: 3.9 for FO case, 3.8 for OP case and 4.1 for uniform inflow reference. The turbine operates at a similar power coefficient value for all those operating points. A $-11/3$ decay slope is observed in the inertial range of the PSDs. It is in agreement with the theoretical predictions of Tobin et al. (2015) and the experimental investigations of Chamorro et al. (2015) and Druault et al. (2022). The relative levels between the loads PSDs are also consistent with the fluctuations levels of each inflow condition (Fig. 7). Contrary to uniform flow reference where

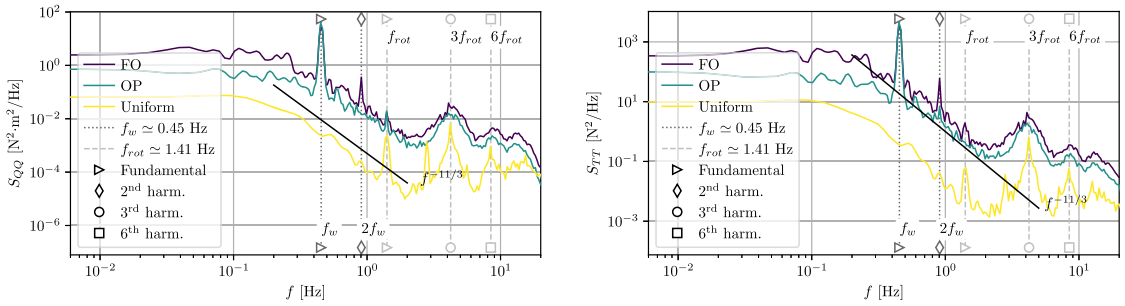


(a) Shaft torque PSDs ($S_{QQ}$). (b) Shaft thrust PSDs ($S_{TT}$).

**Fig. 11** Turbine shaft torque (**a**) and thrust (**b**) PSDs for a single $f_{\text{rot}}$ value corresponding to different $TSR$ for each inflow: 3.9 (FO), 3.8 (OP) and 4.1 (uniform). To ease peak identification, a colour and line-style couple is dedicated to: wave (dark grey dotted line) and rotation (light grey dashed line). Harmonics are indicated with markers: fundamental (triangle), second (diamond), third (circle), sixth (square)

PSDs have a prominent response at the rotation frequency ($f_{\text{rot}}$) and at the second harmonic ($2f_{\text{rot}}$), these peaks appear diluted in the levels of response to turbulent inflow for both wave cases. A common feature for the three considered cases is the significant response at the blades passing frequency of a three-bladed rotor ($3f_{\text{rot}}$). Finally, the general response to both wave cases is very similar. A significant peak at the wave frequency ($f_w$) is noticed for both FO and OP wave cases. The second wave harmonic ($2f_w$) is also discernible in the FO spectra. Its presence will be discussed afterwards.

Figure 11 focuses on loads frequency response in presence of waves at a fixed $TSR$. Nevertheless, a resonance may occur when considering other $TSR$ values. This topic is addressed using the present experimental data because Froude scaling (Eq. (4)) preserves the frequency ratios, meaning that $f_{\text{rot}}/f_w$ is constant between the experiment and real-scale situations. Following the idea proposed by Linant et al. (2025), an adaptation of Campbell diagrams is used. A Campbell diagram generally consists in representing the natural frequencies of a rotating device, identified with ping tests for instance, on top of its measured response in frequency domain at a rotation regime. Here, natural frequencies are replaced by wave-induced forcing ($f_w$ and $2f_w$) and rotation frequencies are displayed in $TSR$ range. Hence, this representation is well suited to identify intercepts between rotation frequencies and wave-related frequencies, indicating possible resonance risk. To enhance (Linant et al. 2025) methodology, a special care is taken on the loads response visualization. To this end, each load PSD (respectively $S_{QQ}$ or $S_{TT}$) is normalized by the load variance (respectively $\sigma_Q^2$ or $\sigma_T^2$). It enables to cross compare results coming from significantly different fluctuations levels. Moreover, as the loads spectra are represented using colour gradient, the decaying nature of the spectra could erroneously mask some peaks of interest. This is the reason why the spectra decay needs to be compensated (i.e. multiplying by the inverse of the decay in inertial range), as performed in some turbulence studies (Blackmore et al. 2016; Durán Medina et al. 2017; Slama et al. 2021). As demonstrated by Tobin et al. (2015), Chamorro et al. (2015) and Druault et al. (2022), the turbine loads perform a double integration of the turbulent spectra. Hence, the resulting torque and thrust spectra are premultiplied by $f^{11/3}$. Those results are gathered in Fig. 12, focusing on OP wave case. Each colour precisely represents a given $TSR$ value. Two operating regimes can be identified. The low $TSR$ regime, which is predominantly blue-coloured, and the high $TSR$ one, predominantly yellow-coloured and characterized by a flat segment that indicates the $-11/3$ decay slope. In between those regimes, the grey curves build a transition from the low $TSR$ regime, of unknown slope, towards the well-established $-11/3$ regime. Moreover, while the $3f_{\text{rot}}$ peak is easily identified in the high $TSR$ regime, it is not discernible in the low $TSR$ regime. The explanation behind this phenomenon is not yet identified and further investigations are needed.

The Campbell diagrams are shown in Fig. 13. FO wave case diagrams are shown in Fig. 13a, b and OP ones are represented in Fig. 13c, d. The colour gradient represents the level of the normalized and compensated spectra. Both wave cases torque shows a response at the rotation frequency ($f_{\text{rot}}$) in the highest $TSR$ domain. It is interpreted as coming from a slight mechanical imbalance of the rotor. However, both torque and thrust respond to the blades passing frequency ($3f_{\text{rot}}$) and second harmonic ($6f_{\text{rot}}$). The associated peaks are well-identifiable for $TSR \geq 3$ but not discernible in the low $TSR$ range. Both torque and thrust respond to wave frequency ($f_w$). While thrust responds at $f_w$ with a similar level across the complete $TSR$ range, torque response increases with $TSR$. Eventually, a response at twice the wave frequency ($2f_w$) is observed for both torque and thrust. A $2f_w$ thrust response across the complete $TSR$ range is observed only in FO conditions (Fig. 13b). Otherwise, both FO and

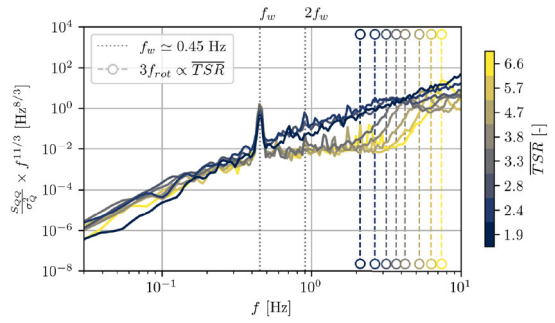


(a) Torque ($S_{QQ} f^{11/3}/\sigma_Q^2$).

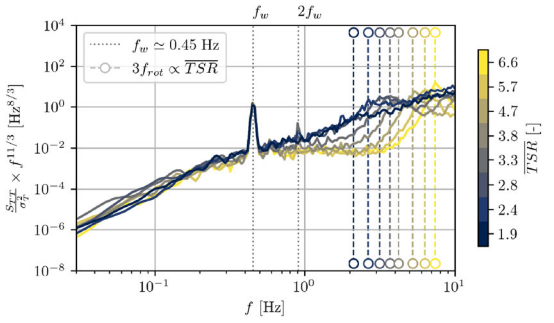


(b) Thrust ($S_{TT} f^{11/3}/\sigma_T^2$).

**Fig. 12** OP wave case normalized and compensated shaft loads spectra: torque (**a**) and thrust (**b**). Different colours represent the $TSR$ associated to each spectra, ranging from low (dark blue) to high (yellow) values. The $3f_{\text{rot}}$ peaks are evidenced using dashed line with circle markers. Wave frequency is reported with dotted dark grey line

OP Campbell diagrams appear very similar. This specific FO response is generated by the presence of $2f_w$ harmonic in upstream flow for $z > z_{\text{rot}}$ as demonstrated in Sect. 5.1. Hence, to simplify the analysis, OP results (Fig. 13c, d) are studied although the same phenomena are also present in FO diagrams (Fig. 13a, b). The $2f_w$ response mainly happens at or near the intercept with the rotation frequency line, indicating a potential resonance. Moreover, twice wave frequency ($2f_w$) response is supported by the theory of the rotational sampling of wave orbital velocities (Draycott et al. 2020). This study by Draycott et al. (2020) highlights that $2f_w$ peak is awaited in blades root bending moment (RBM) PSDs spectra. Moreover, this approach also states that $\pm f_w$ sidebands are expected around the rotation frequency ($f_{\text{rot}}$). The blade root loads measurements performed in the present experiment confirm the presence of both $2f_w$ as well as $\pm f_w$ sidebands around $f_{\text{rot}}$ as shown in Fig. 14. The closeness of $2f_w$ and $f_{\text{rot}} - f_w$ peaks in Fig. 14 shows that possible resonance with twice the wave frequency may also occur for $f_{\text{rot}} > 2f_w$. This last element explains the response observed at $TSR \simeq 3.3$ in OP waves thrust Campbell diagram (Fig. 13d). It shows that the $2f_w$ resonance is not only at risk when $f_{\text{rot}} \sim 2f_w$ but also for higher $TSR$ values that are within the turbine optimal $C_P$ region and where $f_{\text{rot}} - f_w \sim 2f_w$. This is of importance for HATT design as $TSR$ near optimal $C_P$ correspond to real-scale devices operating regimes. Further studies are needed to assess whether this is potentially detrimental. This finding illustrates the relevance of the Campbell diagram representation to identify possible resonances.

## 4 Phase-averaged wake study

The present section focuses on the turbine wake behaviour in relation to surface waves. The LDV flow measurements are performed upstream and downstream of the immersed turbine model at the following $x$-positions: $x/D \in \{-3, -2, -1, -0.5, -0.25, 0.04, 0.25, 0.5, 0.75, 1, 1.5, 2, 2.5, 3, x_{\text{last}}/D\}$. The $x_{\text{last}}$ value respectively equates to $3.74D$ and $4D$ in FO and OP waves due to the geometrical constraint imposed by the damping beach. Measurement points are located every 7.2 cm in the $z$-direction, meaning approximately $0.1D$. To build wake maps and circumvent the scarce spatial discretization of LDV measurements, the flow values are reconstructed between the measurement points using cubic Clough-Tocher interpolation. Each flow velocity acquisition is four-minute long to ensure stochastic convergence. The turbine model rotates at a constant angular velocity during the measurements. The associated $TSR$ (Eq. (17)) is 3.4 in FO waves and 3.3 in OP waves due to the slight difference in reference velocity (Fig. 5).

### 4.1 Wake processing and definitions

The velocity is decomposed using Eq. (10). The sine LMS at wave frequency is not applicable for wake study as higher order harmonics have to be considered. So the phase average with respect to surface waves is performed to evaluate the velocity component at wave frequency (Hussain and Reynolds 1970; Hubert et al. 2025). The complete process of the phase average technique is detailed in Appendix A. The reference motion needed to perform the phase average anal-

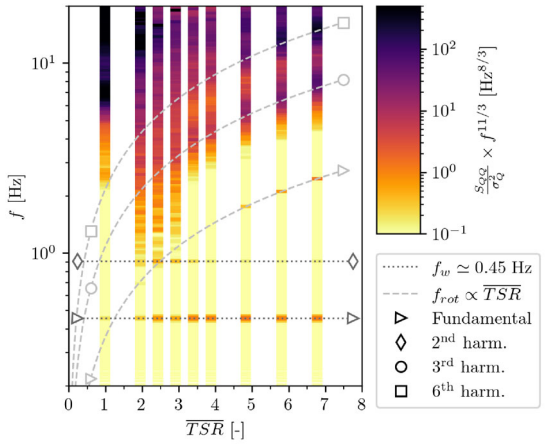


(a) FO, torque.

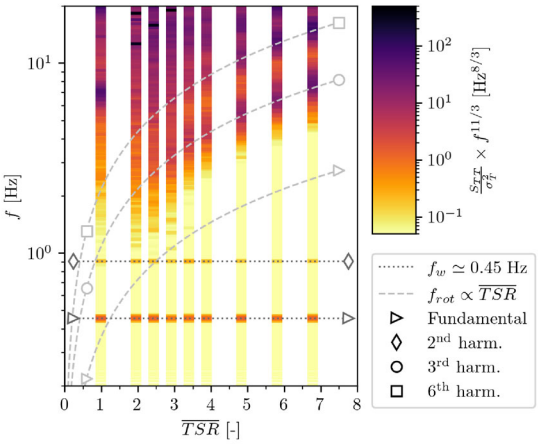


(b) FO, thrust.

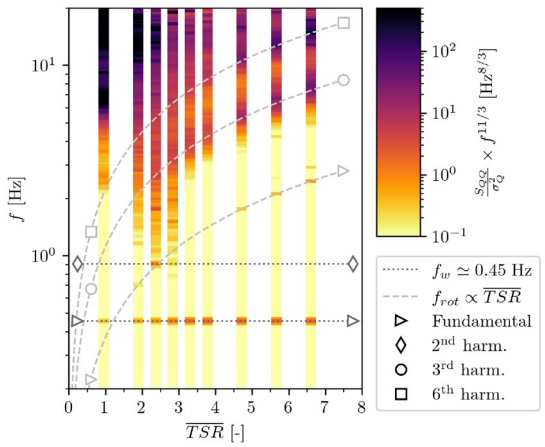


(c) OP, torque.

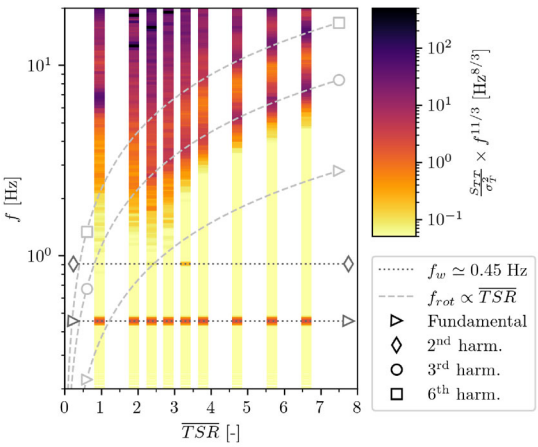


(d) OP, thrust.

**Fig. 13** Campbell diagrams. Normalized and compensated torque (**a**, **c**) and thrust (**b**, **d**) spectra levels are indicated using colour gradient. Top row focuses on FO wave case and bottom row presents OP wave case. Rotation-related harmonics are represented as function of time-averaged $TSR$ with dashed light grey lines: fundamental (triangle), third (circle), sixth (square). The forcing imposed by waves is illustrated via dotted dark grey horizontal lines

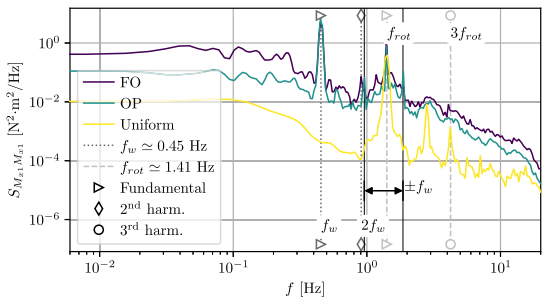


(a) In-plane RBM PSDs ($S_{M_{x1}M_{x1}}$).

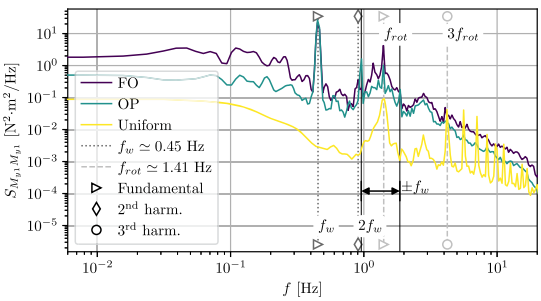


(b) Out-of-plane RBM PSDs ($S_{M_{y1}M_{y1}}$).

**Fig. 14** Blade 1 in-plane (**a**) and out-of-plane (**b**) root bending moment power spectral densities respectively denoted $S_{M_{x1}M_{x1}}$ and $S_{M_{y1}M_{y1}}$. The fixed rotation frequency results in slightly different time-averaged $TSR$ for each inflow case: 3.9 (FO), 3.8 (OP) and 4.1 (uniform). Frequencies of interest are highlighted including $\pm f_w$ sidebands around the rotation frequency ($f_{\text{rot}}$)

ysis is the filtered signal of the free surface elevation from the resistive wave probe B ($\tilde{\eta}_B$). To ensure that the reference phase of the free surface starts at 0° in both FO and OP cases at the rotor $x$-position, wave probe B phase is readjusted following Appendix A.4.3 methodology. Consequently, it is expected to find a trough (respectively a crest) in positive $x$ for FO (respectively OP) wave case.

To study the wake dynamic from a quantitative viewpoint, its boundaries and centroid definitions are introduced. Several methods exist to define wake boundaries from a velocity profile. While the identification of Reynolds stress maxima (Chamorro and Porté-Agel 2009; Tedds et al. 2014; Kang et al. 2014) is a robust technique on finely discretized data, it does not perform as well with moderately resolved data in a sheared inflow. This is the reason why another technique is used in the present study. It consists in detecting when the velocity difference between the characterization reference profile (subscript "$c$") and the local velocity measurements reaches a pre-defined threshold value (Muller et al. 2015; Howland et al. 2016; Hubert et al. 2025). Using this velocity difference enables to circumvent the sheared upstream flow influence on wake boundaries detection. Following multiple studies (España et al. 2011; Howland et al. 2016; Wei et al. 2024; Posa et al. 2024; Hubert et al. 2025), the threshold value ($u_{\text{th}}$) is set as a fraction of a reference velocity. In the present context, the reference velocity is the characterization disc-averaged velocity (Eq. (13)):

$$u_{\text{th}} = 0.15\widehat{\overline{u_{c,x}}}. \tag{22}$$

Wake properties are introduced using surface waves phase-averaged quantities denoted with $\langle\bullet\rangle_w$. The details of the phase averaging process are given in Appendix A. Hence, Eqs. (23) to (25) define the phase-averaged velocity difference ($\langle\Delta u_x\rangle_w$), wake top ($\langle z_t\rangle_w$) and down ($\langle z_d\rangle_w$) boundaries.

$$\langle\Delta u_x\rangle_w(x,z) = \overline{u_{c,x}}(z) - \left[\overline{u_x}(x,z) + \langle u_x\rangle_w(x,z)\right], \tag{23}$$

$\langle z_t\rangle_w$ being defined such that: $\langle z_t\rangle_w > z_{\text{rot}}$ and

$$\langle\Delta u_x\rangle_w(x,\langle z_t\rangle_w) = u_{\text{th}}, \tag{24}$$

$\langle z_d\rangle_w$ being defined such that: $\langle z_d\rangle_w < z_{\text{rot}}$ and

$$\langle\Delta u_x\rangle_w(x,\langle z_d\rangle_w) = \begin{cases} u_{\text{th}} & \text{if } 0 \le x \le 0.8D, \\ 2.2\,u_{\text{th}} & \text{if } x > 0.8D. \end{cases} \tag{25}$$

Wake down limit definition (Eq. (25)) uses a threshold value that depends on $x$-positions. This threshold is increased for $x \ge 0.8D$ to account for the velocity deficit generated by the turbine bottom mounting mast that is not taken into account in the characterization velocity. Mast influence on velocity is not negligible as the mast diameter is comparable to the hub one. Eventually, the phase-averaged wake centroid ($\langle z_{\text{ce}}\rangle_w$) is obtained using the weighted geometric centre method as explained by Muller et al. (2015), Howland et al. (2016) and Hubert et al. (2025):

$$\langle z_{\text{ce}}\rangle_w = \frac{\int_{\langle z_d\rangle_w}^{\langle z_t\rangle_w} z\langle\Delta u_x\rangle_w(x,z)\,\mathrm{d}z}{\int_{\langle z_d\rangle_w}^{\langle z_t\rangle_w} \langle\Delta u_x\rangle_w(x,z)\,\mathrm{d}z}. \tag{26}$$

Second, as a matter of comparison in the study, the time-averaged wake top ($\overline{z_t}$) and down ($\overline{z_d}$) boundaries as well as wake centroid ($\overline{z_{\text{ce}}}$) are also defined. Those quantities are assessed using the phase-averaged definitions (Eqs. (24) to (26)) but applied on the time-averaged velocity difference:

$$\overline{\Delta u_x}(x,z) = \overline{u_{c,x}}(z) - \overline{u_x}(x,z). \tag{27}$$

### 4.2 Phase-averaged wake results and discussion

Figure 15 represents phase-averaged velocity maps with respect to surface waves motion at rotor $x$-position. Velocity results are normalized by the reference disc-averaged value for each inflow condition (Eq. (13)). Figure 15a, c, e, g (respectively Fig. 15b, d, f, h) represents the FO (respectively OP) wave case across four wave phases, starting from 0° up to 270° with 90° increment. The associated phase-averaged turbine wake boundaries and centroid (Eqs. (23) to (26)) are shown in white. Dashed lines indicate wake boundaries ($\langle z_t\rangle_w$ and $\langle z_d\rangle_w$). Dash-dot lines indicate wake centroid ($\langle z_{\text{ce}}\rangle_w$). The farthest wake contours points in Fig. 15f, g are omitted because wake boundaries definitions (Eq. (24) and Eq. (25)) fail to provide results at some phases. This is a known limitation of the methodology (Trujillo et al. 2011; España et al. 2011) which is due to the use of an arbitrary threshold (Eq. (22)). Further work will encompass applying other wake detection techniques such as Gaussian fitting of the velocity deficit (Trujillo et al. 2011; Abraham et al. 2021; Gambuzza and Ganapathisubramani 2023), convolution with a Gaussian kernel (Coudou et al. 2018) or finding Reynolds stress maxima on spatially refined data (Chamorro and Porté-Agel 2009; Tedds et al. 2014; Kang et al. 2014). The time-averaged wake boundaries ($\overline{z_t}$ and $\overline{z_d}$) and centroid ($\overline{z_{\text{ce}}}$) are presented in black for comparison purpose. However, the reader is invited to note that those black contours are not related to the coloured velocity maps.

First, the velocity values near the free surface in Fig. 15 are physically interpreted. This analysis ensures that orbital velocities are consistent with wave phases obtained from the free surface kinematic (Eq. (A14)). For FO wave case, the 0° phase (Fig. 15a) demonstrates a velocity decrease near the free surface for $x \ge 0$. As the waves propagate following the current, towards positive $x$, it denotes a wave trough in the $x \ge 0$ direction. It is then consistent with sine free surface description of Eq. (A14). Accordingly, the 180° phase (Fig. 15e) shows a velocity increase, indicating a wave crest

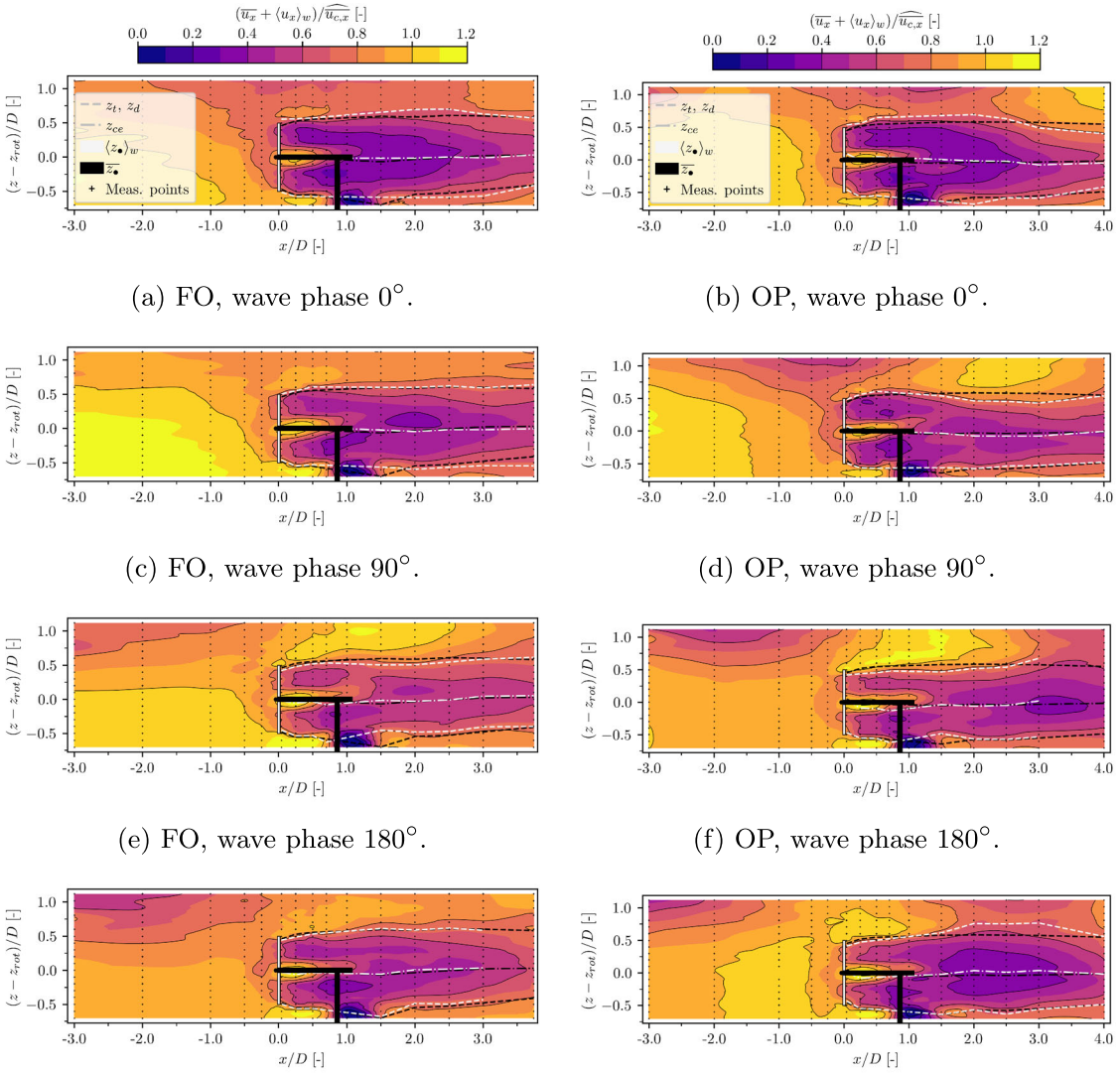


(a) FO, wave phase 0°. (b) OP, wave phase 0°.

(c) FO, wave phase 90°. (d) OP, wave phase 90°.

(e) FO, wave phase 180°. (f) OP, wave phase 180°.

(g) FO, wave phase 270°. (h) OP, wave phase 270°.

**Fig. 15** Maps of phase-averaged velocity with respect to surface waves motion ($\overline{u_x} + \langle u_x \rangle_w$). Velocity is normalized by the disc-averaged reference value ($\widehat{u_{c,x}}$). The flow velocity and associated turbine wake, highlighted in white ($\langle z_t \rangle_w$, $\langle z_d \rangle_w$, $\langle z_{ce} \rangle_w$), are taken at four distinct wave phases: 0° (**a**, **b**), 90° (**c**, **d**), 180° (**e**, **f**), 270° (**g**, **h**). Time-averaged wake quantities ($\overline{z_t}$, $\overline{z_d}$, $\overline{z_{ce}}$) are shown in black as a matter of comparison. Both FO and OP wave cases are presented

in the $x \geq 0$ direction. Similarly, the 0° phase in OP wave case (Fig. 15b) shows a velocity decrease near the free surface for $x \geq 0$. As the waves propagate opposing the current direction, towards negative $x$, it denotes a wave crest in the $x \geq 0$ direction. Hence, it is also consistent with free surface description of Eq. (A14). In the same manner, the OP case 180° phase (Fig. 15f) shows a velocity increase in the $x \geq 0$ direction, denoting a wave trough.

Wake top location ($\langle z_t \rangle_w$) is significantly uplifted and wake down location ($\langle z_d \rangle_w$) is slightly descended when orbitals generate a velocity decrease over the turbine wake. It corresponds to wave trough (respectively crest) passing in FO (respectively OP) conditions. It is mainly discernable at 0° phase for both FO and OP waves (Fig. 15a, b). It is also well noticeable at 270° phase in OP conditions (Fig. 15h) due to a shorter wavelength. On the contrary, $\langle z_t \rangle_w$ (respectively $\langle z_d \rangle_w$) is descended (respectively uplifted) with an orbital velocity increase over the turbine wake. It corresponds to a wave crest in FO conditions (Fig. 15e) and to a wave trough in OP conditions (Fig. 15b, d, f). Wavelength influence on wake boundaries ($\langle z_t \rangle_w$ and $\langle z_d \rangle_w$) motion is hence evidenced by Fig. 15. The FO long wavelength leads to wake boundaries moving simultaneously with waves across all studied $x$-positions. On the contrary, the short wavelength

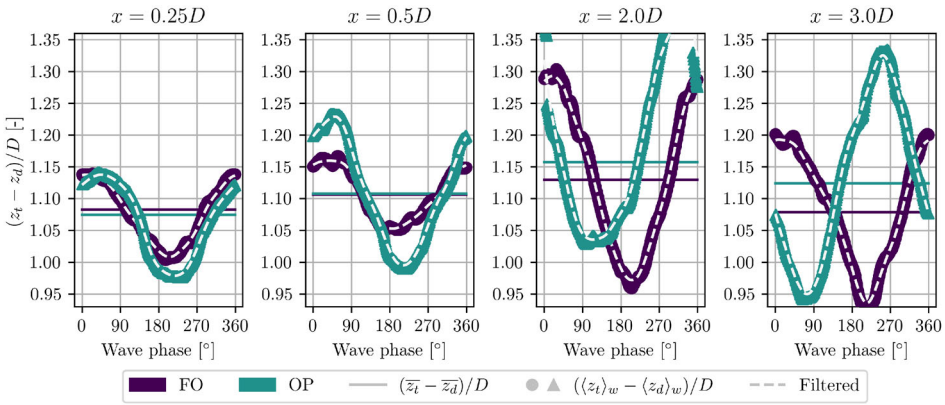


**Fig. 16** Phase-averaged vertical wake width ($\langle z_t \rangle_w - \langle z_d \rangle_w$) fluctuations with respect to surface waves motion. Both wave case are presented: FO (dark purple circle) and OP (blue triangle). From left to right, four $x$-positions downstream of the turbine are studied: $x/D \in \{0.25, 0.5, 2, 3\}$. Time-averaged wake width ($\overline{z_t} - \overline{z_d}$) is represented by means of horizontal lines for comparison

in OP conditions induces phase shifts between wake boundaries motion at different $x$-positions. It is easily discernable in Fig. 15b where wake extension reaches a maximum for $0.5D \leq x \leq 1.5D$ while it reaches a minimum for $x \geq 3D$. Therefore, the wave-induced wake boundaries motion is understood as resulting from the orbital velocity perturbation surrounding the wake which changes the location of threshold velocity detection.

This interpretation is reinforced by analysing the phase-averaged vertical wake width ($\langle z_t \rangle_w - \langle z_d \rangle_w$) fluctuations as a function of wave phase. Results are presented for different $x$-positions in Fig. 16. In the near wake domain ($x/D \in \{0.25, 0.5\}$), wake widths associated to both wave cases are in-phase. At these $x$-positions, wake width maximum is reached between 45° to 90°. It approximately corresponds to the phase of the minimum in FO (respectively maximum in OP) orbital streamwise velocity at these locations. It agrees with the previous description of wake boundaries kinematic. The wake width minimum is reached about 180° degrees after the maximum. Both FO and OP show a similar trend. However for $x$-positions farther in the wake ($x/D \in \{2, 3\}$), a phase shift occurs between FO and OP wake widths fluctuations. This phase shift demonstrates that wave-induced wake width variations are driven by the orbital velocity perturbation surrounding the wake. As previously explained, this phase shift is generated by the wavelength difference between the two wave cases. And this interpretation is tested as it provides a way to evaluate the phase shift magnitude via the formula: $360\Delta x/L_w$ in degrees. It is assessed on the maximum $x$-positions extent: from $0.25D$ to $3D$. The formula gives a phase shift of 45° in FO conditions which is not easily noticeable given the signal shape and the $x$-axis size in Fig. 16. Over the same position extent, the formula provides a phase shift of 150° in OP wave conditions which agrees with Fig. 16 results. To summarise, the wake boundaries variations are driven by orbital $x$-velocity perturbation surrounding the wake.

Following the approach undertaken for the wake width analysis, the phase-averaged wake centroid variations with wave phases are studied. The relative (i.e. without the time-averaged contribution) phase-averaged wake centroid ($\langle z_{ce} \rangle_w - \overline{z_{ce}}$) is presented in Fig. 17. Contrary to wake width, there is no phase shift between FO and OP conditions across the four $x$-positions. It means that wave-induced centroid motion remains in-phase with its emission by the turbine. This observation indicates that wave-induced centroid motion is driven by the time-varying dynamics of the rotor due to orbital velocity inflow perturbation. It is, hence, resulting from a different mechanism than wave-induced wake width fluctuations. For each $x$-positions, both FO and OP wave-induced centroid motion simultaneously shift of phase origin. This change in phase origin is due to the advection of the centroid position at the wake velocity. At $x = 0.25D$, the amplitude of this wave-induced centroid motion is of 6% (respectively 12%) of turbine diameter ($D$) in FO (respectively OP) conditions. Maximum amplitude reaches about 9% of $D$ (respectively 18% of $D$) in FO (respectively OP) conditions at $x = 3D$ (respectively $x = 0.5D$). The highest centroid motion amplitude is reached in OP conditions. It may be linked to the greater $z$-component orbital amplitude in OP waves (Fig. 6a) influencing rotor dynamic. Lastly, it is inferred that this wave-induced wake centroid motion must alter the meandering development. Direct measurement of this phenomenon is not accessible with the present data as $x$-positions are not far enough downstream of turbine. Nevertheless, a parallel can be drawn with floating offshore wind turbines (FOWT) wake analysis as wave-induced inflow perturbation is, to some extent, comparable to a combined surge and heave motions. Experimental measurements from Messmer et al. (2024) and Hubert et al. (2025) as well as numerical results from Li et al. (2022) on FOWT reported comparable coherent centroid motions in turbine wake. Possible synchronisation of wake meandering depending on the inflow perturbation frequency are evidenced in those studies. Further investigation will determine whether similar phe-

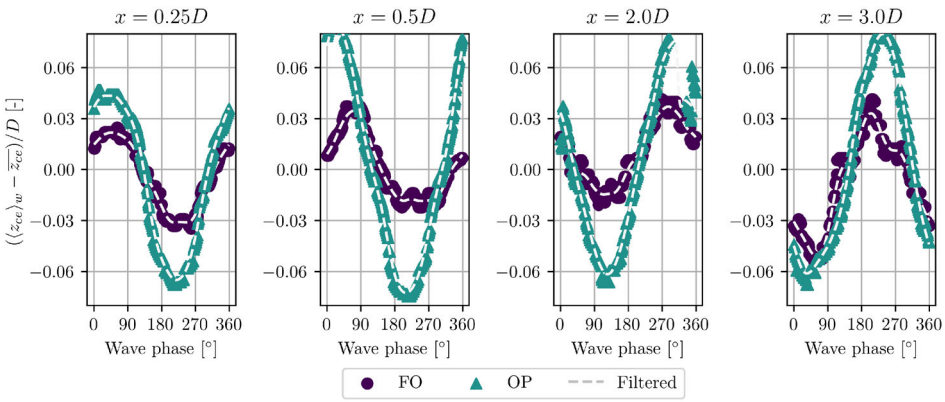


**Fig. 17** Phase-averaged wake centroid relative motion ($\langle z_{ce}\rangle_w - \overline{z_{ce}}$) with respect to surface waves are presented for both conditions: FO (dark purple circle) and OP (blue triangle). From left to right, four $x$-positions downstream of the turbine are studied: $x/D \in \{0.25, 0.5, 2, 3\}$

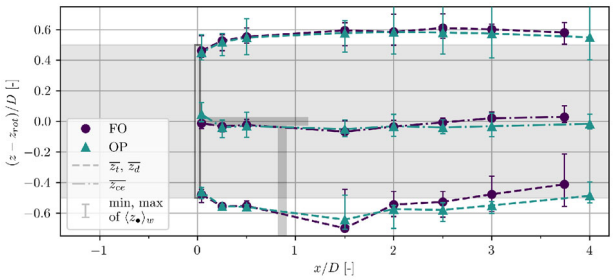


**Fig. 18** Time-averaged wake boundaries ($\overline{z_t}$ and $\overline{z_d}$) together with time-averaged wake centroid ($\overline{z_{ce}}$) from both wave cases: FO (dark purple circle) and OP (blue triangle). The minimum and maximum of each phase-averaged wake property ($\langle z_\bullet\rangle_w$) are specified with error bars

nomenon may be observed in HATT wakes under surface waves.

A final question remains to be tackled. Is there any difference introduced between FO and OP wave cases on the time-averaged wake boundaries ($\overline{z_t}$ and $\overline{z_d}$) and centroid ($\overline{z_{ce}}$)? To answer this question, the time-averaged wake boundaries and centroid (shown in black lines in Fig. 15) are gathered in Fig. 18. The results highlight that there is no significant difference on the time-averaged wake properties between FO and OP wave conditions. FO wave case seems to slightly enhance wake recovery with the most difference appearing in the bottom shear layer. However, this assertion needs additional evaluation with data further downstream of the turbine and transport terms analysis as performed by Ouro et al. (2024), Posa et al. (2024) and Vahidi and Porté-Agel (2024). An extended range of waves characteristics would also be beneficial. Time-averaged wake properties are supplemented with phase-averaged minima and maxima indicated with error bars in Fig. 18. While $\langle z_t\rangle_w$ appears more sensitive to OP wave condition, $\langle z_d\rangle_w$ fluctuations are higher in FO condition. This is related to the difference in amplitude of the $x$-component orbital velocity between rotor top and bottom (shown in Fig. 6a). Finally, the bottom mounting mast influence on lower wake boundary ($\overline{z_d}$) detection is evidenced. In spite of the adapted velocity threshold (Eq. (25)), no result is found at $x = 1D$ and the detection remains affected at $x = 1.5D$ which is not considered as a valid point. As previously mentioned, other wake detection techniques may provide improved results with respect to this issue.

## 5 Wake energy spectra and analytical description

The major advantage of LDV measurements lies in its high temporal resolution enabling to perform frequency analysis. In this section, the energy injection frequencies are studied by means of velocity pre-multiplied power spectral densities (denoted $fS_{u_xu_x}$) at a TSR of 3.4 in FO waves and 3.3 in OP waves (Eq. (17)). This approach has already been used in previous numerical and experimental studies to identify the flow energy content in turbine wakes (Chamorro et al. 2012; Toloui et al. 2015; Dong et al. 2023; Gambuzza and Ganapathisubramani 2023; Vahidi and Porté-Agel 2024).

### 5.1 Wake energy spectra measurements

In the present study, velocity PSDs are computed using an in-house implementation of Welch (1967) algorithm. The signals are cut into segments of $2^{11}$ elements with half-width overlapping. Hann window is used to reduce Gibbs phenomenon and spectral leakage. Zero padding enhances the results discretization. Those signal processing parameters influence peaks magnitude. The logarithmic scale is used to represent the pre-multiplied spectra ($fS_{u_xu_x}$) levels as an improved readability of peaks and frequencies of interest has been noticed.

Figure 19 shows the pre-multiplied velocity spectra ($fS_{u_xu_x}$) with levels represented by means of a colour scale. The normalized depth ($(z - z_{rot})/D$) is reported on the $y$-axis and the $x$-axis represents the frequency range. On the one hand, FO wave conditions results are displayed on left

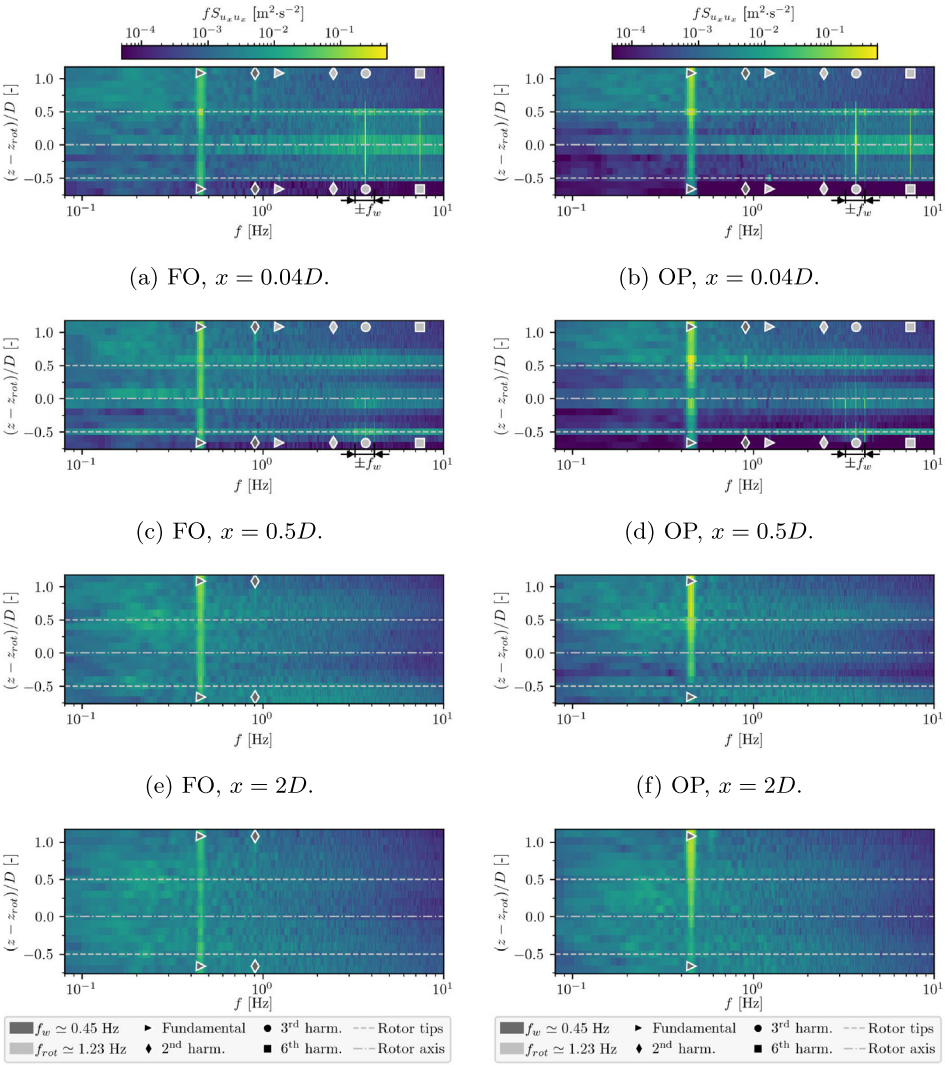


(a) FO, $x = 0.04D$. (b) OP, $x = 0.04D$.

(c) FO, $x = 0.5D$. (d) OP, $x = 0.5D$.

(e) FO, $x = 2D$. (f) OP, $x = 2D$.

(g) FO, $x = 3.74D$. (h) OP, $x = 4D$.

**Fig. 19** Pre-multiplied velocity PSDs ($f S_{u_x u_x}$) as function of depth ($(z - z_{\text{rot}})/D$). The colour scale indicates the spectra level. FO (left column) and OP (right column) results are shown at different $x$-positions: $0.04D$ (**a**, **b**), $0.5D$ (**c**, **d**), $2D$ (**e**, **f**), and respectively $3.74D$ (**g**) and $4D$ (**h**). Harmonics of interest are highlighted with markers: fundamental (triangle), second (diamond), third (circle), sixth (square) coloured with respect to waves (dark grey) or rotation (light grey)

column (Fig. 19a, c, e, g) for $x$-positions being respectively $0.04D$, $0.5D$, $2D$, $3.74D$. On the other hand, OP wave conditions results are displayed on right column (Fig. 19b, d, f, h) for $x$-positions being respectively $0.04D$, $0.5D$, $2D$, $4D$. The farthest position slightly differs between FO and OP due to damping beach geometric constraint in the flume tank. Differentiating between wave frequency ($f_w$) and rotation frequency ($f_{\text{rot}}$) using line styles would have hindered the figure readability. This is the reason why a change of markers colour is preferred: wave-related harmonics are shown in dark grey while rotation-related harmonics are shown in light grey. Markers edges are white to increase contrast with any colour of the map behind. Last, the rotor swept area is highlighted with dashed lines for tips and dash-dot lines for its centre.

First, surface waves orbital velocity signature is present in Fig. 19 for both wave cases throughout all studied $x$-positions. They are identified by means of the wave frequency ($f_w$) which distinctly appears. The $f_w$ frequency spans across all water depths with an increasing level close to the free surface. This variation with respect to depth is more visible in OP wave conditions which agrees with orbital velocity profiles shown in Fig. 6a. Moreover, in FO conditions, the second wave harmonic ($2f_w$) is present in the free surface vicinity. This second harmonic highlights the flume tank undesired response to the imposed FO conditions which are at the edge of its capabilities.

Second, the turbine signature is evidenced. From a macro scale point of view, the turbine injects energy across a frequency range from 1 Hz to higher than 10 Hz. This energy increase located within rotor limits is noticed immediately downstream of turbine at $x = 0.04D$ (Fig. 19a, b). This energy injection is even more pronounced at the blade roots and tips. While at first well-contained within turbine limits,

this injected energy progressively diffuses in the flow with increasing $x$-positions. At the farthest $x$-positions (Fig. 19g, h), there is no distinctive turbine signature in the flow except an increased energy level at all depths. For $x \geq 0.8D$ (Fig. 19e, f, g, h), part of the energy increase in the lower half of turbine swept area ($z \leq z_{\text{rot}}$) results from bottom mounting mast influence. However, it does not affect previous conclusions.

Third, to describe the characteristics of the energy injected by the turbine, specific frequencies only present for $x/D \in \{0.04, 0.5\}$ (Fig. 19a, b, c, d) are thoroughly analysed. At $x = 0.04D$, an interaction between upper tip vortices and waves is noticed for both FO and OP conditions (Fig. 19a, b). It generates an increase of the energy contained at $f_w$ frequency in the upper blade tip region. This phenomenon is also discernable at $x = 0.5D$ mainly for OP conditions. Furthermore, at the blade tips, slight $f_{\text{rot}}$ and $2f_{\text{rot}}$ frequency peaks are visible. There presence is also reported in the literature (Chamorro et al. 2012; Toloui et al. 2015; Biswas and Buxton 2024a; Posa et al. 2024). Those frequencies are associated to tip vortices merging process (Toloui et al. 2015; Eriksen and Krogstad 2017; Biswas and Buxton 2024a). Eventually, for both wave cases, frequencies directly associated to tip vortices are of significant level, namely: the number of blades times rotation frequency ($3f_{\text{rot}}$), also known as blades passing frequency, and twice this frequency ($6f_{\text{rot}}$). At $x = 0.04D$ (Fig. 19a, b), they span along the complete rotor swept area. At $x = 0.5D$ (Fig. 19c, d), they are, however, limited to root and tip vortices regions. Those frequencies are in good agreement with other studies performed on three-bladed turbines (Chamorro et al. 2012; Toloui et al. 2015; Dong et al. 2023; Biswas and Buxton 2024a; Posa et al. 2024). A striking element of the present study is the $\pm f_w$ sidebands associated to $3f_{\text{rot}}$ and $6f_{\text{rot}}$ frequencies. Such sidebands may either be generated by frequency modulation or by triadic interactions (Baj and Buxton 2017; Biswas and Buxton 2024b). Only the former origin is investigated here. Yet, the study of triadic interactions will require thorough investigations in upcoming works. It is then hypothesised that tip vortices (responsible for the $3f_{\text{rot}}$ and $6f_{\text{rot}}$ frequencies) are modulated by the waves orbital velocity field. Such a phenomenon must be visible only before the tip vortices break up. The significant turbulence levels in the present experiment (Fig. 6b) explains why $3f_{\text{rot}}$ and $6f_{\text{rot}}$ frequencies with associated sidebands can only be observed in the very near wake. To confirm the relevance of this modulation hypothesis, an analytical vortex model will be derived and presented in Sect. 5.2.

Figure 20 presents the pre-multiplied spectra of Fig. 19 in a more classical manner to ease the comparison with the analytical vortex model afterwards. The pre-multiplied spectra of Fig. 20 are extracted at two specific $z$-positions: in the top tip vortices vicinity at $z - z_{\text{rot}} = 0.5D$ (Fig. 20a, b) and in the middle of the blade span at $z - z_{\text{rot}} = 0.3D$ (Fig. 20c, d). The $x$-positions are represented using four different colours. It starts with black at $x = 0.04D$ and fades into the respective colour dedicated to FO (purple) or OP (blue) wave conditions with increasing $x$-values. Spectra are shown up to $2D$ inasmuch as no noticeable elements are evidenced from Fig. 19 on farthest available downstream spectra. The reference spectra, coming from measurements at $x = -3D$ (i.e. farthest upstream of turbine), are highlighted in green. Turbine injects more energy in the tip vortices region (Fig. 20a, b) than in the middle of blade span area (Fig. 20c, d). It is in line with previous studies conclusions (Chamorro et al. 2012; Dong et al. 2023). Furthermore, compared to reference spectra level (green curves), results of Fig. 20a, b confirm that the wave frequency ($f_w$) energy increases in the tip vortices region ($z - z_{\text{rot}} = 0.5D$) immediately downstream of turbine ($x/D \in \{0.04, 0.5\}$). At $x = 0.04D$, the $3f_{\text{rot}}$ and $6f_{\text{rot}}$ frequencies are well identifiable for both $z$-positions. Lastly, at $x = 0.04D$, the $\pm f_w$ sidebands around both $3f_{\text{rot}}$ and $6f_{\text{rot}}$ are also evidenced. Those sidebands are of prominent magnitude at $z - z_{\text{rot}} = 0.5D$ and of smaller amplitude at $z - z_{\text{rot}} = 0.3D$. An explanation of their presence is proposed in the following Sect. 5.2.

### 5.2 Idealized analytical vortex model to explain wave frequency sidebands

To provide an analysis of the $\pm f_w$ sidebands, experimentally evidenced around $3f_{\text{rot}}$ and $6f_{\text{rot}}$, an analytical vortex model of the wake is implemented. The wake model consists in idealized semi-infinite vortex helices issuing from each blade tip. The quasi steady model, initially formulated by Corniglion et al. (2022) for step changes in the flow, is adapted to the present situation. A periodic modification of each helix is introduced to account for waves orbital influence. It constitutes a modulation of the tip vortex helices by the wave orbitals velocity field. Each tip vortex helix modified by surface waves can be seen as a slinky helical spring with a wave travelling through.

Let $t \in \mathbb{R}$ be a given time, $t_h \in \mathbb{R}$ the parameter describing each helix and $N_B$ the number of blades. Each helix is indexed by $k \in [\![0, N_B - 1]\!]$ starting at zero for calculus convenience. An element position of the $k$-th helix is defined by $\vec{x}_k$. In the present analytical model, it is assumed that the tip vortices mean convection velocity is the flow upstream velocity ($u^\infty$). Although a better accuracy is achievable (Wood and Boersma 2001; Okulov and Sørensen 2010; Corniglion et al. 2022), this hypothesis significantly simplifies the present model without impairing the results quality in frequency domain. The model modification lies in including waves orbital velocity $x$-component in the tip vortices convection velocity. The choice to neglect waves orbital velocity $z$-component is made to keep the model as simple as possible.

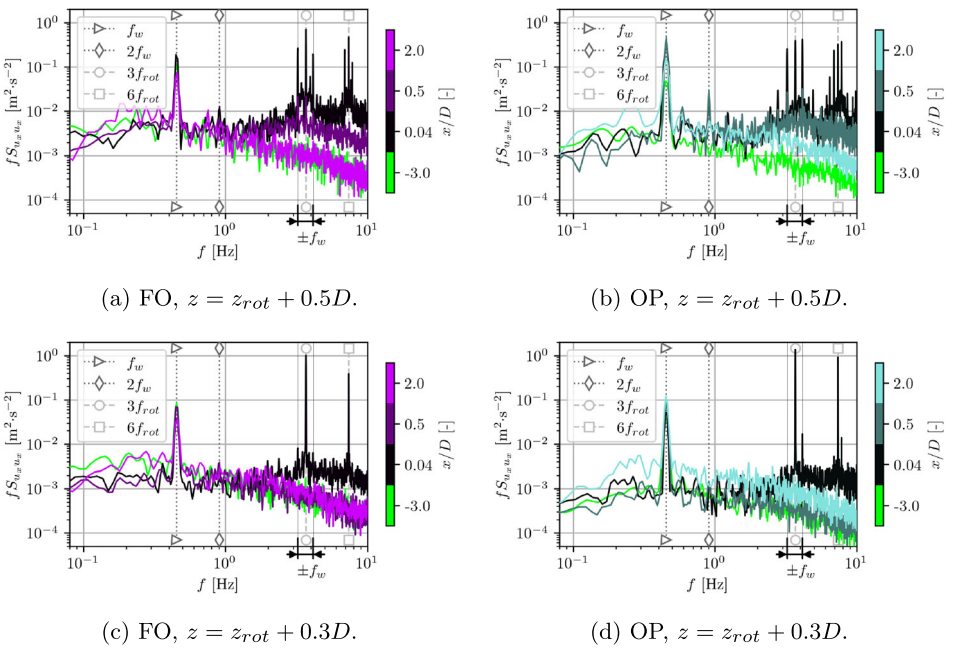


(a) FO, $z = z_{rot} + 0.5D$. (b) OP, $z = z_{rot} + 0.5D$.

(c) FO, $z = z_{rot} + 0.3D$. (d) OP, $z = z_{rot} + 0.3D$.

**Fig. 20** Velocity pre-multiplied PSD spectra at two different depths for both wave cases: FO (left column) and OP (right column). One depth is in the upper tip vortices region at $z - z_{\text{rot}} = 0.5D$ (**a**, **b**) and the other one is close to the middle of the blade span at $z - z_{\text{rot}} = 0.3D$ (**c**, **d**). The four different colours indicate the $x$-position of each spectra. Wave-related (dark grey dotted lines) and rotation-related (light grey dashed lines) harmonics are highlighted with markers specified in the legend

It also enables to verify the minimal set of hypothesis needed to reproduce the experimental results. It means that only the $x$-direction of the helix position is affected by waves, contrary to the $z$-direction which remains unchanged. The orbitals amplitude is simplified to omit the $z$-dependency. It is hence defined as $u^{\infty}\mu^{w}$ using the current number (Eq. (15)). Surface waves orbital $x$-component velocity is described by means of Stokes first order model (Peregrine 1976; Molin 2023) as defined in Eq. (14). The wave phase term is position-dependent as detailed in Appendix A.4.3. Evaluating this term at the element position of the $k$-th helix ($\vec{x}_k$) would impose a sub-iteration process because this position depends itself on the orbital velocity that includes the phase term. To circumvent this issue and keep the model quasi steady, only the helix average position (equating to $u^{\infty}t_h$) is used in the waves orbital velocity formulation. The scope is here restricted to FO and OP wave cases, meaning that the propagation angle is: $\beta \in \{0°, 180°\}$. All those elements provide a definition for this idealized element position of the $k$-th helix vortex ($\vec{x}_k$) affected by waves presence:

$$\vec{x}_k = \begin{pmatrix} u^{\infty}t_h + u^{\infty}t_h\mu^{w}\sin\left(\omega_w t - k_w\cos(\beta)u^{\infty}t_h\right) \\ R\cos\left(\omega_{\text{rot}}(t+t_h) + 2\pi k/N_B\right) \\ z_{\text{rot}} + R\sin\left(\omega_{\text{rot}}(t+t_h) + 2\pi k/N_B\right) \end{pmatrix}. \tag{28}$$

Following the approach proposed by Corniglion et al. (2022), the velocity induced by the tip vortex helices ($\vec{u}^{\,i}$) at any point in space ($\vec{x}$) is evaluated using the Biot–Savart law:

$$\vec{u}^{\,i}(\vec{x},t) = -\frac{\Gamma}{4\pi}\sum_{k=0}^{N_B-1}\int \frac{\vec{x}-\vec{x}_k}{\|\vec{x}-\vec{x}_k\|^3}\times \mathrm{d}\vec{x}_k, \tag{29}$$

where $\Gamma$ represents the tip vortex circulation assumed to be constant along each helix. This circulation is of negative value due to sign convention of Biot–Savart law. It is evaluated by means of the Kutta–Joukowski theorem:

$$\Gamma = -\frac{1}{2}c_{95}C_L\sqrt{(u^{\infty})^2 + R^2\omega_{\text{rot}}^2}, \tag{30}$$

with $c_{95}$ the blade chord at 95% of blade length (available in Dufour et al. (2024a) work), $C_L$ the lift coefficient, and an estimate of the relative velocity at blade tip. Using a constant circulation is a common feature in similar helical vortex models (Hardin 1982; Segalini and Alfredsson 2013; Abraham et al. 2023). It implies to also keep the lift coefficient constant. It seems a reasonable assumption given the limited angle of attack fluctuations near blade tip for similar flow conditions with waves (Dufour et al. 2024b; Smyth et al. 2025). Given the angle of attack value near blade tip and polar curves provided by Dufour et al. (2024a), the lift coefficient ($C_L$) is fixed at a value of 1. To simplify the assessment of Eq. (29), the evaluation position ($\vec{x}$) is constrained in the middle plane ($\vec{e}_x, 0, \vec{e}_z$), meaning $\vec{x} = (x, 0, z)$. To describe each helix by means of the one-dimensional parameter $t_h$, a change of variable is performed under the integral of Eq. (29). This is done by injecting Eq. (28) into Eq. (29) and by using $\mathrm{d}\vec{x}_k/\mathrm{d}t_h$ derivative. Focusing on the $x$-component of the induced velocity ($u_x^i$) provides the final formulation:

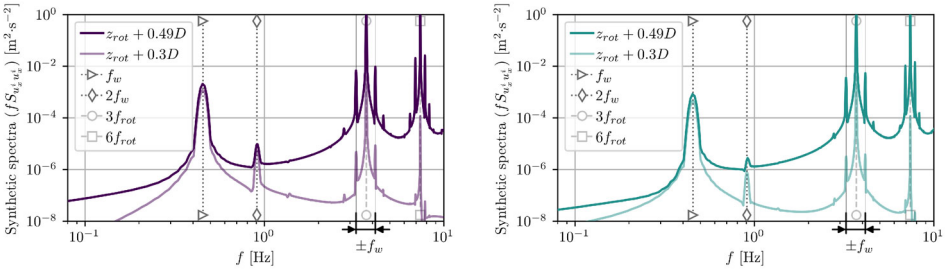


(a) FO wave case.

(b) OP wave case.

**Fig. 21** Synthetic pre-multiplied PSD spectra of the velocity induced by the wave-modulated helical vortices ($fS_{u_x^i u_x^i}$). Those are synthetic spectra from the analytical model. Two different depths are investigated: near top tip vortices at $z - z_{\text{rot}} = 0.49D$ (dark lines) and in the middle of blade span at $z - z_{\text{rot}} = 0.3D$ (light lines). The two wave conditions are reproduced: FO (**a**) and OP (**b**)

$$
\begin{aligned}
u_x^i(x,z,t) &= \vec{u}^i \cdot \vec{e}_x \\
&= -\frac{\Gamma}{4\pi} \sum_{k=0}^{N_B-1} \int_0^{+\infty} \frac{\omega_{\text{rot}} R}{\|\vec{x} - \vec{x}_k\|^3} \big[-R \\
&\quad + (z - z_{\text{rot}}) \sin\left(\omega_{\text{rot}}(t + t_h) + 2\pi k/N_B\right)\big] \mathrm{d}t_h, \qquad (31) \\
\|\vec{x} - \vec{x}_k\|^3 &= \big[x^2 + (u^\infty t_h)^2 \big(1 + (\mu^w)^2 \sin^2\left(\omega_w t - k_w \cos(\beta) u^\infty t_h\right)\big) \\
&\quad - 2x u^\infty t_h + R^2 + (z - z_{\text{rot}})^2 \\
&\quad + 2u^\infty t_h \mu^w \left(u^\infty t_h - x\right) \sin\left(\omega_w t - k_w \cos(\beta) u^\infty t_h\right) \\
&\quad - 2(z - z_{\text{rot}}) R \sin\left(\omega_{\text{rot}}(t + t_h) + 2\pi k/N_B\right)\big]^{3/2}. \qquad (32)
\end{aligned}
$$

Equation (31) is evaluated at positions $\vec{x} = (0.04D, 0, z)$ such that $(z - z_{\text{rot}})/D \in \{0.3, 0.49\}$. Those evaluation positions refer to the experimental ones presented in Fig. 20. The evaluation position $z - z_{\text{rot}} = 0.49D$ is chosen to avoid the singularity in Eq. (31) while remaining similar to $0.5D$. Hence, the resulting synthetic spectra can be compared to Fig. 20 black curves ($x = 0.04D$). The integral of Eq. (31) is numerically evaluated with an upper bound set to reach a converged value. In practice, at the studied $x$-position, this upper bound is $4D/u^\infty$. Equation (31) induced velocity is assessed on ninety-second time arrays sampled at 200 Hz. The resulting pre-multiplied PSDs of the induced velocity ($fS_{u_x^i u_x^i}$) are presented in Fig. 21. As the synthetic spectra do not account for direct orbital velocities contribution (only the modulation of tip vortices position is accounted for) nor turbulence-induced fluctuations, the obtained energy levels are different from measurements (Fig. 20). Complete synthetic spectra would require adding orbital velocity field using parameters described in Table 3 and Appendix B.1 as well as a synthetic turbulent contribution using inputs from Appendix B.2. At $z - z_{\text{rot}} = 0.49D$, near the tip vortices, significant $\pm f_w$ sidebands for both FO and OP wave cases are evidenced at $3f_{\text{rot}}$ and $6f_{\text{rot}}$. At $z - z_{\text{rot}} = 0.3D$, the sidebands are of lower amplitude around $3f_{\text{rot}}$ and even barely noticeable for $6f_{\text{rot}}$. All those elements concur with the trends observed in experimental measurements (Fig. 20). It highlights the ability of the presented vortex model to capture the physics behind the sidebands. Consequently, the modulation of the tip vortices position by the surface waves orbital velocity field appears to accurately describe the sidebands. For the sake of explanation, the phenomenon can be depicted as a wave travelling along a slinky helical spring. Investigating the possibility to describe this modulation process using vortex-pairing instabilities (Ivanell et al. 2010; Abraham et al. 2023; Wei et al. 2024) is part of future works.

## 6 Conclusions

This study presents experimental results on a three-bladed horizontal axis tidal turbine model immersed in a wave and current flume tank. It focuses on surface waves influence on both turbine loads and wake dynamics. Two wave conditions are investigated depending on the propagation direction. The first wave case propagates following (FO) current direction and the second one propagates opposing (OP) current direction. Waves amplitude and period are set via Froude scaling based on measured conditions at tidal stream energy sites.

A thorough characterization of inflow conditions is performed to enable reproducibility of the experiment. Waves and turbulence contributions are isolated to evaluate orbital velocities amplitude and turbulent fluctuations. Flow properties are averaged over the turbine rotor swept area (disc-averaged) when applicable. It better quantifies the conditions experienced by the turbine as they vary with depth. Orbital velocity amplitudes are assessed using the current number. It is the ratio of disc-averaged orbital $x$-velocity amplitude divided by the disc-averaged upstream mean $x$-velocity. Current number reaches 11% in FO and 8% in OP waves conditions. The disc-averaged 3D turbulence intensity equates to 9% in FO and 5% in OP conditions. Supplements to waves (wavelength assessment and exact frequency) and turbulence

(Reynolds stress components and integral length scale) properties are given in Appendix B.

For the considered wave cases, a very limited wave effect is observed on turbine average performance. However, performance fluctuations are significantly increased by waves. Prior studies evidenced that performance fluctuations are proportional to velocity fluctuations. This relation is all the more verified for low frequency velocity perturbations, which is the case of wave orbital velocities. Hence, it is shown here that the performance fluctuations in monochromatic wave conditions are scaled by the current number which quantifies the relative amplitude of $x$-component orbital velocity. Furthermore, the frequency domain response of loads (torque or thrust) is investigated. It is performed using power spectral densities (PSD) of the load normalized by its variance and compensated for the decay in inertial range. On the one hand, it is evidenced that the decay slope in the inertial range is dependent upon the turbine tip speed ratio (TSR). The optimum to over-speed regimes show the well-known $-11/3$ decay slope in logarithmic scale. However, low TSRs reveal a smaller slope responsible for higher fluctuations levels. On the other hand, those normalized and compensated PSDs of the loads are analysed by means of Campbell diagrams in frequency-TSR domain. Those diagrams demonstrate that both torque and thrust respond to waves with a similar relative magnitude except for low TSR where torque response decreases. Furthermore, Campbell diagrams provide insights on possible resonance. Twice the wave frequency ($2f_w$) is at risk when it equates either the rotation frequency ($f_{\text{rot}}$) or an associated sideband ($f_{\text{rot}} - f_w$). The second forcing frequency being the most detrimental one as it is close to the turbine optimal operating point.

Concerning the turbine wake study, there is no significant difference between FO and OP wave cases on the spatial boundaries of time-averaged wake in the turbine vicinity. However, positions farther downstream have to be studied to confirm the trend at $4D$ where the bottom shear layer starts to differ. Moreover, velocity is phase-averaged using waves motion as reference. Phase-averaged wake is then used to identify wave-induced wake kinematic. FO wave trough and OP wave crest, both induce a velocity decrease leading to an increase of the wake width. On the contrary, FO wave crest and OP wave trough, both inducing a velocity increase, are associated to a decrease of wake width. Hence, the wave-induced fluctuations of wake width are understood as resulting from the local orbital velocity perturbation surrounding the wake. This viewpoint also explains the phase shift measured on wave-induced wake width variations between FO and OP wave cases due to the difference in wavelengths. As opposed to wake width variations, wave-induced wake centroid motion is driven by the time-varying dynamics of the rotor due to orbital velocity inflow perturbation. Centroid motion amplitude is respectively up to 9% and 18% of rotor diameter in FO and OP conditions.

Finally, the spectral signature of the turbine wake is studied using pre-multiplied velocity PSDs. High energy levels are injected by the turbine over a wide band of frequencies ranging from 1 Hz to 10 Hz. The preferred areas of energy injection are concentrated at blade roots and tips as it is where most of the vorticity is shed in the flow. Moreover, specific frequencies associated to tip vortices are evidenced: the blades passing frequency ($3f_{\text{rot}}$) and its second harmonic ($6f_{\text{rot}}$). Those frequencies are visible only in the immediate vicinity of the turbine. At the closest $x$-position, where the vorticity lattice shed by the blades is clearly defined, $3f_{\text{rot}}$ and $6f_{\text{rot}}$ frequencies are noticed over the complete blade span. The higher energy levels are at first well-contained within rotor limits but they progressively spread in the flow. Hence, at about four diameters downstream, the turbine signature is not discernable any longer. In addition, specific interactions between turbine wake and waves are evidenced. In the vicinity of the upper tip vortices, a localised increase of the spectrum magnitude is observed at the wave frequency ($f_w$). Around both $3f_{\text{rot}}$ and $6f_{\text{rot}}$ frequencies, wave-induced sidebands are evidenced. Their bandwidth equates the wave frequency ($\pm f_w$). Those sidebands are interpreted as a modulation of tip vortices by wave orbital velocity. Eventually, to confirm this interpretation, an analytical vortex model of the turbine wake is proposed. Tip vortices helices are modified by $x$-component wave orbital velocity. Results of this vortex model concur with the experimental observation: increased magnitude at $f_w$ and $\pm f_w$ sidebands around $3f_{\text{rot}}$ and $6f_{\text{rot}}$. The modulation phenomenon can be depicted as a wave travelling through a slinky helical ring spring, symbolizing each tip vortex helix.

The first part of future works can be performed without additional data. Reynolds stress and other wake detection techniques ought to be studied. Moreover, other mechanisms to describe the wave-induced sidebands in the wake needs to be explored: triadic interactions, vortex-pairing instabilities. In a second phase, the database can be supplemented by broadening the range of studied waves. To this end, more wave cases and upstream velocities need to be considered. This wider range of current numbers could emphasize on possible wave influences that have not been evidenced in the present study. Furthermore, as the present wake study focuses only on optimal TSR value, more turbine operating points have to be considered to evaluate the influence of the ratio between the wave frequency and the rotation frequency.

## Appendix A: Periodic velocity component theoretical aspects and processing

The Reynolds decomposition splits the velocity between a steady average component ($\overline{\vec{u}}$) and a turbulent component ($\vec{u}'$). If a $T$-periodic zero-mean motion is present in the flow, this decomposition is supplemented with an associated component ($\vec{u}^p$) following (Hussain and Reynolds 1970). Let $\vec{x}_0 \in \mathbb{R}^3$ be a fixed spatial point in the flow. It reads:

$$\vec{u}(\vec{x}_0, t) = \overline{\vec{u}}(\vec{x}_0) + \vec{u}^p(\vec{x}_0, t) + \vec{u}'(\vec{x}_0, t). \tag{A1}$$

Following Eq. (A1) decomposition, the main question is: how to properly assess the $T$-periodic zero-mean velocity component ($\vec{u}^p$)? The present appendix aims at providing some answers to this question.

### A.1 Fourier series decomposition

Let $\bullet$ be any spatial direction ($x$, $y$ or $z$). Fourier series decomposition theorem provides the existence of amplitude ($A_k(u^p_\bullet)(\vec{x}_0)$) and phase ($\varphi_k(u^p_\bullet)(\vec{x}_0)$) coefficients to write the given periodic signal as an infinite sum of sine components, $k$-index starting at 1 as the considered signal is of zero mean:

$$u^p_\bullet(\vec{x}_0, t) = \sum_{k=1}^{+\infty} A_k(u^p_\bullet)(\vec{x}_0) \sin\left(2\pi \frac{k}{T} t + \varphi_k(u^p_\bullet)(\vec{x}_0)\right). \tag{A2}$$

### A.2 Time discretized viewpoint

The numerically resampled LDV velocity data are of sampling frequency $f_e = 1/T_e$ with $T_e$ being the sampling period. So the time ($t$) is discrete. A fixed integer ($N_e \in \mathbb{N}$) exists such that the total acquisition time is $N_e T_e$. The recorded velocity signal, for any spatial component ($\bullet$) is a sequence:

$$(u_\bullet(\vec{x}_0, mT_e))_{m\in[\![1,N_e]\!]}, \tag{A3}$$

with $t = mT_e$. Let a complete time period ($T$) be discretized into $N_p \in \mathbb{N}$ points. Depending on the chosen method to evaluate the periodic velocity component, the time period may be oversampled meaning:

$$\frac{T}{N_p} \leq T_e. \tag{A4}$$

How to properly assess $\left(u^p_\bullet(\vec{x}_0, nT/N_p)\right)_{n\in[\![1,N_p]\!]}$ from the measurement data $(u_\bullet(\vec{x}_0, mT_e))_{m\in[\![1,N_e]\!]}$? Originally, Hussain and Reynolds (1970) proposed the phase average technique. This technique is presented in Appendix A.4.1. While this method surely provides the awaited result, it may not be applicable depending on the experimental set-up. This is the reason why another technique easier to apply, at the cost of lower precision and robustness, is presented in Appendix A.3: the sine least mean square (LMS) at known frequency.

### A.3 Sine least mean square (LMS) at known frequency

If the periodic component looked for is purely sinusoidal (Eq. (A2) with $k = 1$), and if its frequency ($1/T$) is a priori exactly known, the sine least mean square (LMS) at known frequency process (Jacquelin 2014) can be applied on the band-pass-filtered (Tisserand et al. 2009; Legrand 2013) measured signal $((\tilde{u}_\bullet(\vec{x}_0, mT_e))_{m\in[\![1,N_e]\!]})$ to extract coefficients $A_1$ and $\varphi_1$. It consists in the very same principle as described in Sect. 2.2.2 for wave probes processing.

$$u^p_\bullet(\vec{x}_0, nT/N_p) = A_1(u^p_\bullet)(\vec{x}_0) \sin\left(2\pi \frac{n}{N_p} + \varphi_1(u^p_\bullet)(\vec{x}_0)\right). \tag{A5}$$

### A.4 Phase average process

If higher order harmonics are not negligible, or if the experimental set-up allows to record a $T$-periodic reference motion, the phase average technique should be applied. First introduced by Hussain and Reynolds (1970), the technique has since been applied to study wind turbine wakes (Eriksen and Krogstad 2017; Hubert et al. 2025) and tidal turbines loads under surface waves (Lust et al. 2013; McNaughton et al. 2025).

#### A.4.1 Phase average technical aspects

The $T$-periodic reference motion is defined as: $(r(mT_e))_{m\in[\![1,N_e]\!]}$. To remove any disturbing noise, this signal is numerically filtered at frequency ($1/T$) using in-house second-order band pass filters (Legrand 2013; Tisserand et al. 2009) providing $(\tilde{r}(mT_e))_{m\in[\![1,N_e]\!]}$. The obtained filtered signal is assumed to be either a pure sine or pure cosine. The associated complex-valued analytic signal (Oppenheim and Schafer 2014) is:

$$\tilde{r}_a(mT_e) = \mathcal{F}^{-1}\left[(1 + \mathrm{sgn})\mathcal{F}\left[\tilde{r}\right]\right](mT_e), \tag{A6}$$

with $\mathcal{F}$ and $\mathcal{F}^{-1}$ respectively denoting the Fourier transform and its inverse. The sign function (sgn) is defined with the half-maximum convention, meaning it outputs zero for input zero. Fourier transform is performed by means of an in-house fast Fourier transform (FFT) algorithm (Cooley and Tukey

1965; Oppenheim and Schafer 2014). As a complex number, the analytic signal (Eq. (A6)) can be immediately rewritten with an amplitude ($E_r(mT_e)$) and phase ($\xi_r(mT_e)$):

$$\tilde{r}_a(mT_e) = E_r(mT_e)e^{\mathrm{i}\xi_r(mT_e)}. \tag{A7}$$

The phase signal ($(\xi_r(mT_e))_{m\in[\![1,N_e]\!]}$) corresponds to the instantaneous phase of the filtered reference motion. A $+\pi/2$ offset is added to the phase signal if the reference motion is a pure sine. See Oppenheim and Schafer (2014) for details. Hence, for any time ($t = mT_e$) and any position ($\vec{x}_0$), a velocity value ($u_\bullet(\vec{x}_0, mT_e)$) is associated to a phase value ($\xi_r(mT_e)$) of the reference motion wrapped on the $]0, 2\pi]$ radians range. The $]0, 2\pi]$ radians range is arbitrarily discretized into $N_p$ points, see Eq. (A4) and Appendix A.2. Let a local phase be $\xi = n2\pi/N_p$ with $n \in [\![1, N_p]\!]$. Following (Hubert et al. 2025), the phase averaged velocity associated to this precise reference motion phase ($\xi$) is defined as:

$$\langle u_\bullet\rangle_p(\vec{x}_0, \xi) = \frac{\sum_{m=1}^{N_e}\left(u_\bullet(\vec{x}_0, mT_e) - \overline{u_\bullet}(\vec{x}_0)\right)K_h(\Delta\xi_m)}{\sum_{m=1}^{N_e}K_h(\Delta\xi_m)}, \tag{A8}$$

with a special attention paid to the domain periodicity to correctly define the phase difference ($\Delta\xi_m$):

$$\Delta\xi_m = \begin{cases} |\xi - \xi_r(mT_e)| & \text{if } |\xi - \xi_r(mT_e)| \le \pi, \\ 2\pi - |\xi - \xi_r(mT_e)| & \text{otherwise,} \end{cases} \tag{A9}$$

and where weighting kernel ($K_h$) is the Epanechnikov function detailed by García-Portugués (2025):

$$K_h(\Delta\xi_m) = \begin{cases} \frac{3}{4h_\xi}\left(1 - \left(\frac{\Delta\xi_m}{h_\xi}\right)^2\right) & \text{if } \Delta\xi_m \le h_\xi, \\ 0 & \text{otherwise.} \end{cases} \tag{A10}$$

The half bandwidth parameter is set as $h_\xi = 10°$. The obtained phase average ($\langle u_\bullet\rangle_p(\vec{x}_0, \xi)$, Eq. (A8)) answers the problem of finding the periodic velocity component ($u_\bullet^p(\vec{x}_0, nT/N_p)$). While the notation $u_\bullet^p(\vec{x}_0, nT/N_p)$ denotes the periodic velocity component which can either be obtained from sine LMS at known frequency or from the phase average process, the notation $\langle u_\bullet\rangle_p(\vec{x}_0, \xi)$ remains reserved for phase average result.

### A.4.2 Illustration of phase average process

An example is presented to demonstrate the capabilities of the phase average process previously described (see Appendix A.4.1). The synthetic input data used in the present example are built using the following parameters: $N_e = 10^4$, $f_e = 120$ Hz, $1/T = 2.3$ Hz. The reference motion signal is defined as:

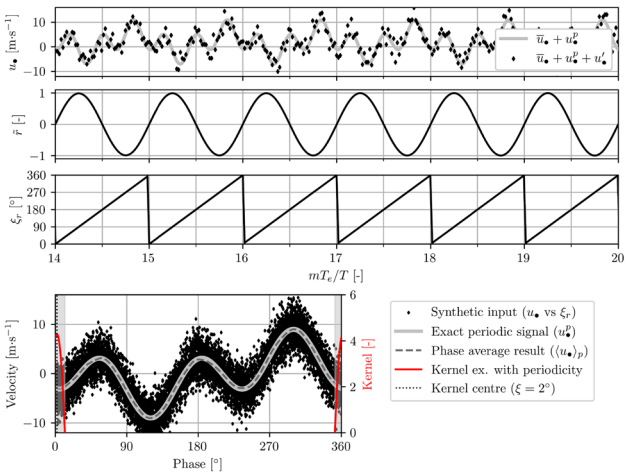


**Fig. 22** Illustration of the complete phase average process and control of its accuracy on a synthetic dataset

$$r(mT_e) = \sin\left(\frac{2\pi}{T}mT_e\right). \tag{A11}$$

Following the velocity decomposition (Eq. (A1)) and Fourier series (Eq. (A2)), the synthetic velocity signal is arbitrarily defined as:

$$\begin{aligned} u_\bullet(\vec{x}_0, mT_e) = {} & \underbrace{2}_{=\overline{u}_\bullet(\vec{x}_0)} \\ & \underbrace{+4\cos\left(\frac{2\pi}{T}mT_e + \frac{\pi}{3}\right) + 5\cos\left(3\left(\frac{2\pi}{T}mT_e + \frac{\pi}{3}\right)\right)}_{=u_\bullet^p(\vec{x}_0, mT_e)} \\ & + u'_\bullet(\vec{x}_0, mT_e). \end{aligned} \tag{A12}$$

Python's *numpy.random.default_rng().normal(scale)* function is used to imitate turbulence influence ($u'_\bullet$) in Eq. (A12). The *scale* parameter is arbitrarily set as $scale = \sqrt{f_e/20}$. In Eq. (A12), the periodic component is a function of $mT_e$ as it is unwrapped on the complete signal length. This component is voluntarily chosen with a fundamental frequency ($1/T$) and an harmonic at three times this fundamental. It illustrates the phase average process capability to accurately capture higher order harmonics contrary to sine LMS at known frequency. Lastly, this periodic component is defined with a phase shift with respect to the reference signal phase. It represents a more general case with, for instance, LDV position changes along $\vec{e}_x$ axis introducing phase shifts.

The complete phase average process using the presented synthetic data is summarized in Fig. 22. First, in the upper graph of Fig. 22, a snippet over six time periods ($T$) of the synthetic velocity input ($u_\bullet$, Eq. (A12)) is presented. In the

second graph of Fig. 22, the synthetic band-pass-filtered reference signal ($\tilde{r}$, Eq. (A11)) is shown. The pure sine reference motion is unaltered by the filtering operation. In the third graph of Fig. 22, the phase ($\xi_r$, Eq. (A7)) resulting from the analytic signal of the filtered reference motion is shown. It is wrapped on the ]0, 360] degrees range. And it is consistently phased with the upper sine reference signal ($\tilde{r}$, Eq. (A11)). Eventually, in the last graph of the figure, the full synthetic velocity ($u_\bullet$, Eq. (A12)) is plotted against the phase ($\xi_r$, Eq. (A7)). It is represented with the black diamond markers and named "Synthetic input". On top of that, the exact periodic signal from the synthetic input data (thick medium grey line named "Exact periodic signal", Eq. (A12)) is shown. The phase average result ($\langle u_\bullet \rangle_p$, Eq. (A8)), plotted with a dark grey dashed line named "Phase average result", evidences a very good agreement with respect to the exact periodic signal. This shows the capability of the phase average process to capture the fundamental as well as any higher harmonics in the periodic component. Lastly, an example of Epanechnikov kernel (Eq. (A10)) is shown for a two degrees local phase ($\xi$). The values taken by the Epanechnikov kernel are represented with the red line named "Kernel ex. with periodicity" and its centreline at $\xi = 2°$ is the black dotted line. This local phase of two degrees is shown to highlight the domain periodicity and the correct behaviour of the phase difference definition (Eq. (A9)). Figure 22 proved to be helpful in finely tuning the kernel half window width ($h_\xi$).

#### A.4.3 Phase shift of waves reference motion

The waves reference motion used to perform the phase average process is the filtered free surface elevation from the resistive wave probe B ($\tilde{\eta}_B$). However, as this wave probe is not located at rotor $x$-position, using directly the associated phase signal would compromise results analysis. This is the reason why a specific phase shift term depending on wave probe position has to be added. It is assumed that the surface waves propagate following a wave number vector ($\vec{k}_w$) that may not be aligned with the current. This wave number vector forms an angle $\beta \in ]-\pi, \pi]$ with respect to the current direction ($\vec{e}_x$) such that:

$$\vec{k}_w = k_w \cos(\beta)\vec{e}_x + k_w \sin(\beta)\vec{e}_y, \tag{A13}$$

with $k_w = 2\pi/L_w$. Only FO and OP wave cases are studied meaning $\beta \in \{0°, 180°\}$. Stokes first order wave and current model (Peregrine 1976; Molin 2023) supplements the wave probe signal definition given in Eq. (7) with position-dependent phase term such that:

$$\begin{aligned}\tilde{\eta}_B(t) &= a_B \sin\left(\omega_w t - \vec{k}_w \cdot \vec{x}_B\right) \\ &= a_B \sin(\omega_w t - k_w \cos(\beta) x_B)\,.\end{aligned} \tag{A14}$$

FO and OP wave cases experience significantly different wave numbers. Hence, Eq. (A14) demonstrates that very different phases at time origin between FO and OP conditions are obtained at wave probe B location. To enable the cross comparison between FO and OP wave cases, a solution is to set wave phase at zero above the rotor $x$-position, meaning $x = 0$ m. This is the reason why $k_w \cos(\beta) x_B$ term is added to the phases output modifying both FO and OP phase signals to start at 0° at rotor location.

## Appendix B: Supplement to upstream conditions characterization

Supplements to the description of the upstream flow and the free surface conditions are provided here. This is done in particular to enable any numerical fluid dynamicist to reproduce the described experiment.

### B.1 Surface waves frequency and wavelength

As mentioned in Sect. 2.2.2, the wave maker slightly changes the reference frequency ($1/T_w^\infty$). Its working principle is based on fitting as much as possible of complete wave periods within a 64 s range. Hence, the relation between the reference frequency ($1/T_w^\infty$) and the wave frequency ($f_w$) in the experiment is:

$$f_w = \frac{\lfloor 64/T_w^\infty \rceil}{64}. \tag{B16}$$

Moreover, a second insight on the waves properties concerns the wavelength ($L_w$) evaluation. A double verification of the wavelength values (Table 3 in Sect. 2.2.2) provided by the LMS phase difference is performed. To this end, another method is used to assess wavelengths. The purpose of this second method is to involve directly unfiltered signals, meaning $\eta_A$ and $\eta_C$. The time delay ($\Delta t_{AC}$) is evaluated using the cross-correlation between $\eta_A$ and $\eta_C$. Let $\tau_e$ be the time of the first cross-correlation extrema. Then, $\Delta t_{AC} = \tau_e$ if the extrema is a maxima, $\Delta t_{AC} = T_w/2 - \tau_e$ otherwise. It provides a completely independent wavelength evaluation process. This cross-correlation method is applied on the same dataset as in Sect. 2.2.2. The resulting wavelengths are $L_w \simeq 4.7$ m for the OP wave case, thus validating the LMS-obtained value, and $L_w \simeq 12.7$ m for the FO wave case. This change in the FO wavelength comes from the very small considered time delay. This is due to the limited spacing between probes A and C which results itself from spatial constraints. Hence, the evaluation of the time delay ($\Delta t_{AC}$) may be altered enough to change the resulting wavelength (Eq. (8) in Sect. 2.2.2). This uncertainty on the FO

**Table 4** Turbine disc-averaged turbulence properties

| Wave case | $\widehat{\sigma^2_{u'_{c,x}}}$ [m$^2$ s$^{-2}$] | $\widehat{\sigma^2_{u'_{c,y}}}$ [m$^2$ s$^{-2}$] | $\widehat{\sigma^2_{u'_{c,z}}}$ [m$^2$ s$^{-2}$] | $\widehat{L_I}$ [m] |
|---|---|---|---|---|
| FO | $7.2 \times 10^{-3}$ | $5.3 \times 10^{-3}$ | $5.2 \times 10^{-3}$ | 0.6 |
| OP | $2.7 \times 10^{-3}$ | $2.1 \times 10^{-3}$ | $2.0 \times 10^{-3}$ | 0.4 |

wavelength value should be considered when numerically reproducing the present experiment.

## B.2 Parameters to synthetically reproduce turbulence

For the turbulence description to be complete, more properties ought to be described: Reynolds stress tensor and integral length scale ($L_I$). Firstly, the Reynolds stress tensor components are studied. A focus is made on the Reynolds stress tensor diagonal terms ($\sigma^2_{u'_{c,x}}, \sigma^2_{u'_{c,y}}, \sigma^2_{u'_{c,z}}$). Disc integrated values (denoted $\widehat{\bullet}$, see Sect. 2.2.3) of the diagonal terms are reported in Table 4. Those diagonal terms are one to two orders of magnitude greater than symmetric non-diagonal ones, except for $\overline{u'_{c,x}u'_{c,z}}$ which is two to three times lower only. It raised concern among the authors questioning the waves orbital component complete removal from turbulence. To check on this, magnitude square coherences (Carter et al. 1973) between each of the three turbulent components have been computed. For both wave case, a very low coherence level between $u'_{c,x}$ and $u'_{c,z}$ components is found at wave frequency ($f_w$). Thus, it invalidates the hypothesis of a partial removal of wave component. However, a relatively high level of coherence (with values ranging from 0.4 to 0.8) at frequencies lower than 0.1 Hz is found between $u'_{c,x}$ and $u'_{c,z}$ components. This high response at low frequency is not observed in the MSC of other turbulent components couples. To the authors viewpoint, it can be interpreted as the flume tank partial standing wave mode response previously mentioned. Hence, according to the authors, this mode does not interfere in the presented results as presented wave orbitals are very similar to other similar experiments (Lust et al. 2013; Guo et al. 2018; McNaughton et al. 2025). It should then not be taken into account in turbulence synthetic modelling. This is the reason why only the diagonal components of the Reynolds stress tensor are provided in Table 4. Secondly, the integral length scale ($L_I$) representing the eddies size that contains the biggest part of turbulent energy (Tennekes and Lumley 1972; Roy et al. 2004; Blackmore et al. 2016) is evaluated. Let $\tau_0$ be the time for the turbulent velocity autocorrelation function ($R(u'_{c,x})$) to reach the threshold value ($\pm 0.02$) around zero (see Fig. 8 in Sect. 2.2.3). The integral time scale is obtained by performing the integration of the autocorrelation function between zero and $\tau_0$ (Blackmore et al. 2016). Then it is assumed that only convection affects the eddy throughout the considered time, which is known as Taylor's frozen eddy hypothesis. It yields:

$$L_I(z) = \overline{u_{c,x}}(z) \int_0^{\tau_0} R(u'_{c,x}(z))(\tau)\, \mathrm{d}\tau. \tag{B17}$$

Disc-averaged integral length scale values for both wave conditions are summarized in Table 4. It is important to note from Fig. 8 that keeping wave component in the turbulent part would significantly affect the evaluation of the integral length scale. In the authors opinion, this proves the necessity to separate waves component from the velocity signal when assessing upstream conditions.

**Acknowledgements** The authors would like to thank Jean-Valery Facq for the experimental set-up design and for his valuable advice and presence throughout the experiment. Moreover, the authors acknowledge the support of Benoît Gomez and Nabila Ahssayni who conducted part of the presented measurements. In addition, the authors express their gratitude towards the reviewers whose advice and comments contributed to enhance the present manuscript.

**Author Contributions** M.A.D. wrote the main manuscript text with associated analysis, developed the major part of the data processing tools and prepared the figures. B.G. contributed to the data processing tools, the analysis and the experiment conceptualization. G.G. and G.P. conceptualized the experiment, contributed to the analysis and were in charge of project management and funding acquisition. All authors edited and reviewed the manuscript.

**Funding** Open access funding provided by Université Le Havre Normandie. The present research is co-funded by the Normandy Region and IFREMER as part of a PhD project. This work has also received funding from the French government, the Hauts-de-France Region and IFREMER via the CPER IDEAL framework agreement.

**Data availability** The data that support the findings of this study are available online from a public SEANOE repository (Dufour et al. 2025).

## Declarations

**Conflict of interest** The authors have no conflict of interest to declare that are relevant to the content of this article.

## References


Abraham A, Martínez-Tossas LA, Hong J (2021) Mechanisms of dynamic near-wake modulation of a utility-scale wind turbine. J Fluid Mech 926:A29. https://doi.org/10.1017/jfm.2021.737

Abraham A, Castillo-Castellanos A, Leweke T (2023) Simplified model for helical vortex dynamics in the wake of an asymmetric rotor. Flow 3:5. https://doi.org/10.1017/flo.2022.33

Bahaj AS, Molland AF, Chaplin JR, Batten WMJ (2007) Power and thrust measurements of marine current turbines under various hydrodynamic flow conditions in a cavitation tunnel and a towing tank. Renew Energy 32(3):407–426. https://doi.org/10.1016/j.renene.2007.10.001

Baj P, Buxton ORH (2017) Interscale energy transfer in the merger of wakes of a multiscale array of rectangular cylinders. Phys Rev Fluids 2(11):114607. https://doi.org/10.1103/PhysRevFluids.2.114607

Barltrop N, Varyani KS, Grant A, Clelland D, Pham X (2006) Wave-current interactions in marine current turbines. Proc Inst Mech Eng Part M J Eng Marit Environ 220(4):195–203. https://doi.org/10.1243/14750902JEME45

Barltrop N, Varyani KS, Grant A, Clelland D, Pham XP (2007) Investigation into wave-current interactions in marine current turbines. Proc Inst Mech Eng Part A J Power Energy 221(2):233–242. https://doi.org/10.1243/09576509JPE315

Bell SA (2001) A beginner's guide to uncertainty of measurement. Measurement Good Practice Guide 1568, Centre for Basic, Thermal and Length Metrology, National Physical Laboratory, Teddington, Middlesex, United Kingdom

Biswas N, Buxton ORH (2024a) Effect of tip speed ratio on coherent dynamics in the near wake of a model wind turbine. J Fluid Mech 979:34. https://doi.org/10.1017/jfm.2023.1095

Biswas N, Buxton ORH (2024b) Energy exchanges between coherent modes in the near wake of a wind turbine model at different tip speed ratios. J Fluid Mech 996:8. https://doi.org/10.1017/jfm.2024.581

Blackmore T, Myers LE, Bahaj AS (2016) Effects of turbulence on tidal turbines: implications to performance, blade loads, and condition monitoring. Int J Mar Energy 14:1–26. https://doi.org/10.1016/j.ijome.2016.04.017

Bouferrouk A, Hardwick JP, Colucci AM, Johanning L (2016) Quantifying turbulence from field measurements at a mixed low tidal energy site. Renew Energy 87:478–492. https://doi.org/10.1016/j.renene.2015.10.046

Bourgoin ACL, Guillou SS, Thiébot J, Ata R (2020) Turbulence characterization at a tidal energy site using large-eddy simulations: case of the Alderney Race. Philos Trans R Soc A Math Phys Eng Sci 378(2178):20190499. https://doi.org/10.1098/rsta.2019.0499

Carter G, Knapp C, Nuttall A (1973) Estimation of the magnitude-squared coherence function via overlapped fast Fourier transform processing. IEEE Trans Audio Electroacoust 21(4):337–344. https://doi.org/10.1109/TAU.1973.1162496

Chamorro LP, Porté-Agel F (2009) A wind-tunnel investigation of wind-turbine wakes: boundary-layer turbulence effects. Bound-Layer Meteorol 132(1):129–149. https://doi.org/10.1007/s10546-009-9380-8

Chamorro LP, Guala M, Arndt REA, Sotiropoulos F (2012) On the evolution of turbulent scales in the wake of a wind turbine model. J Turbul 13:27. https://doi.org/10.1080/14685248.2012.697169

Chamorro LP, Lee S-J, Olsen D, Milliren C, Marr J, Arndt REA, Sotiropoulos F (2015) Turbulence effects on a full-scale 2.5 MW horizontal-axis wind turbine under neutrally stratified conditions. Wind Energy 18(2):339–349. https://doi.org/10.1002/we.1700

Cooley JW, Tukey JW (1965) An algorithm for the machine calculation of complex Fourier series. Math Comput 19(90):297–301. https://doi.org/10.1090/S0025-5718-1965-0178586-1

Corniglion R, Harris JC, Peyrard C (2022) The aerodynamics of a blade pitch, rotor speed, and surge step for a wind turbine regarding dynamic inflow. Wind Energy 25(5):858–880. https://doi.org/10.1002/we.2702

Coudou N, Moens M, Marichal Y, Van Beeck J, Bricteux L, Chatelain P (2018) Development of wake meandering detection algorithms and their application to large eddy simulations of an isolated wind turbine and a wind farm. J Phys: Conf Ser 1037:072024. https://doi.org/10.1088/1742-6596/1037/7/072024

Dong G, Qin J, Li Z, Yang X (2023) Characteristics of wind turbine wakes for different blade designs. J Fluid Mech 965:15. https://doi.org/10.1017/jfm.2023.385

Draycott S, Payne G, Steynor J, Nambiar A, Sellar B, Venugopal V (2019) An experimental investigation into non-linear wave loading on horizontal axis tidal turbines. J Fluids Struct 84:199–217. https://doi.org/10.1016/j.jfluidstructs.2018.11.004

Draycott S, Steynor J, Nambiar A, Sellar B, Venugopal V (2020) Rotational sampling of waves by tidal turbine blades. Renew Energy 162:2197–2209. https://doi.org/10.1016/j.renene.2020.10.037

Druault P, Gaurier B, Germain G (2022) Spatial integration effect on velocity spectrum: towards an interpretation of the—11/3 power law observed in the spectra of turbine outputs. Renew Energy 181:1062–1080. https://doi.org/10.1016/j.renene.2021.09.106

Dufour M-A, Pinon G, Gaurier B, Germain G, Facq J-V, Togneri M, Represas F, Nicolas E, Marcille J (2022) Comparison of the experimental response of two horizontal axis tidal turbines to wave and current from a frequency dependency point of view. In: Guedes Soares C (ed) Trends in renewable energies offshore, 1st edn. CRC Press, London. https://doi.org/10.1201/9781003360773

Dufour M-A, Pinon G, Rivoalen E, Blondel F, Germain G (2024a) Development and validation of a lifting-line code associated with the vortex particle method software Dorothy. Wind Energy 27(7):633–666. https://doi.org/10.1002/we.2905

Dufour M-A, Germain G, Pinon G, Rivoalen E (2024b) Wave modelling in vortex particle solver Dorothy: a tidal turbine study. In: Actes des 19èmes Journées de l'Hydrodynamique. Comité des Journées de l'Hydrodynamique, Nantes, France

Dufour M-A, Gaurier B, Germain G, Facq J-V, Gomez B, Pinon G (2025) Experimental database of loads and wake of a single horizontal axis tidal turbine (HATT) immersed in two different wave and current conditions. SEANOE. https://doi.org/10.17882/111192

Durán Medina O, Schmitt FG, Calif R, Germain G, Gaurier B (2017) Turbulence analysis and multiscale correlations between synchronized flow velocity and marine turbine power production. Renew Energy 112:314–327. https://doi.org/10.1016/j.renene.2017.05.024

Eriksen PE, Krogstad PÅ (2017) Development of coherent motion in the wake of a model wind turbine. Renew Energy 108:449–460. https://doi.org/10.1016/j.renene.2017.02.031

España G, Aubrun S, Loyer S, Devinant P (2011) Spatial study of the wake meandering using modelled wind turbines in a wind tunnel. Wind Energy 14(7):923–937. https://doi.org/10.1002/we.515

Evans P, Armstrong S, Wilson C, Fairley I, Wooldridge C, Masters I (2013) Characterisation of a highly energetic tidal energy site with specific reference to hydrodynamics and bathymetry. In: Proceedings of the 10th European wave and tidal energy conference (EWTEC). EWTEC Secretariat, Aalborg, Denmark

Faudot C, Dahlhaug OG (2012) Prediction of wave loads on tidal turbine blades. Energy Procedia 20:116–133. https://doi.org/10.1016/j.egypro.2012.03.014

Filipot J-F, Prevosto M, Maisondieu C, Le Boulluec M, Thomson J (2015) Wave and turbulence measurements at a tidal energy site. In: 2015 IEEE/OES eleventh current, waves and turbulence measurement (CWTM). IEEE, St. Petersburg, pp 1–9. https://doi.org/10.1109/CWTM.2015.7098128

Furgerot L, Sentchev A, Bailly du Bois P, Lopez G, Morillon M, Poizot E, Méar Y, Bennis A-C (2020) One year of measurements in Alderney Race: preliminary results from database analysis. Philos Trans R Soc A Math Phys Eng Sci 378(2178):20190625. https://doi.org/10.1098/rsta.2019.0625

Galloway PW, Myers LE, Bahaj AS (2014) Quantifying wave and yaw effects on a scale tidal stream turbine. Renew Energy 63:297–307. https://doi.org/10.1016/j.renene.2013.09.030

Gambuzza S, Ganapathisubramani B (2021) The effects of free-stream turbulence on the performance of a model wind turbine. J Renew Sustain Energy 13(2):023304. https://doi.org/10.1063/5.0039168

Gambuzza S, Ganapathisubramani B (2023) The influence of free stream turbulence on the development of a wind turbine wake. J Fluid Mech 963:19. https://doi.org/10.1017/jfm.2023.302

García-Portugués E (2025) Notes for Nonparametric Statistics, 1st edn. Self-publishing, Madrid, Spain

Gaurier B, Davies P, Deuff A, Germain G (2013) Flume tank characterization of marine current turbine blade behaviour under current and wave loading. Renew Energy 59:1–12. https://doi.org/10.1016/j.renene.2013.02.026

Gaurier B, Ordonez-Sanchez S, Facq J-V, Germain G, Johnstone C, Martinez R, Salvatore F, Santic I, Davey T, Old C, Sellar B (2020) Marinet2 tidal energy round robin tests-performance comparison of a horizontal axis turbine subjected to combined wave and current conditions. J Mar Sci Eng 8(6):463. https://doi.org/10.3390/jmse8060463

Gaurier B, Germain G, Facq J-V (2022) Determination of the response amplitude operator of a tidal turbine as a spectral transfer function. Int Mar Energy J 5(2), 151–160. https://doi.org/10.36688/imej.5.151-160

Guillou N, Chapalain G, Neill SP (2016) The influence of waves on the tidal kinetic energy resource at a tidal stream energy site. Appl Energy 180:402–415. https://doi.org/10.1016/j.apenergy.2016.07.070

Guo X, Yang J, Gao Z, Moan T, Lu H (2018) The surface wave effects on the performance and the loading of a tidal turbine. Ocean Eng 156:120–134. https://doi.org/10.1016/j.oceaneng.2018.02.033

Guy C, Hart E, Vengatesan V, Forehand D (2024) Numerical modelling of a 1.5 MW tidal turbine in realistic coupled wave-current sea states for the assessment of turbine hub-depth impacts on mechanical loads. Ocean Eng 292:116577. https://doi.org/10.1016/j.oceaneng.2023.116577

Hardin JC (1982) The velocity field induced by a helical vortex filament. Phys Fluids 25(11):1949–1952. https://doi.org/10.1063/1.863684

Howland MF, Bossuyt J, Martínez-Tossas LA, Meyers J, Meneveau C (2016) Wake structure in actuator disk models of wind turbines in yaw under uniform inflow conditions. J Renew Sustain Energy 8(4):043301. https://doi.org/10.1063/1.4955091

Hubert A, Conan B, Aubrun S (2025) Spatiotemporal behavior of the far wake of a wind turbine model subjected to harmonic motions: phase averaging applied to stereo particle image velocimetry measurements. Wind Energy Sci 10(7):1351–1368. https://doi.org/10.5194/wes-10-1351-2025

Hussain AKMF, Reynolds WC (1970) The mechanics of an organized wave in turbulent shear flow. J Fluid Mech 41(2):241–258. https://doi.org/10.1017/S0022112070000605

Ivanell S, Mikkelsen R, Sørensen JN, Henningson D (2010) Stability analysis of the tip vortices of a wind turbine. Wind Energy 13(8):705–715. https://doi.org/10.1002/we.391

Jacquelin J (2014) Regressions and integral equations, Scribd edn. Self-Publishing, Paris

Kang S, Yang X, Sotiropoulos F (2014) On the onset of wake meandering for an axial flow turbine in a turbulent open channel flow. J Fluid Mech 744:376–403. https://doi.org/10.1017/jfm.2014.82

Lam R, Dubon SL, Sellar B, Vogel C, Davey T, Steynor J (2023) Temporal and spatial characterisation of tidal blade load variation for structural fatigue testing. Renew Energy 208:665–678. https://doi.org/10.1016/j.renene.2023.03.117

Legrand F (2013) Filtres à réponse impulsionnelle infinie (RII). Informatique Appliquée aux Sciences Physiques. www.f-legrand.fr/scidoc/docmml/numerique/filtre/rii/rii.html#ref1

Lewis MJ, Neill SP, Hashemi MR, Reza M (2014) Realistic wave conditions and their influence on quantifying the tidal stream energy resource. Appl Energy 136:495–508. https://doi.org/10.1016/j.apenergy.2014.09.061

Lewis M, Neill SP, Robins P, Hashemi MR, Ward S (2017) Characteristics of the velocity profile at tidal-stream energy sites. Renew Energy 114:258–272. https://doi.org/10.1016/j.renene.2017.03.096

Li Z, Dong G, Yang X (2022) Onset of wake meandering for a floating offshore wind turbine under side-to-side motion. J Fluid Mech 934:A29. https://doi.org/10.1017/jfm.2021.1147

Linant R, Saouli Y, Germain G, Maurice G (2025) Experimental study of the wave effects on a ducted twin vertical axis tidal turbine wake development. J Mar Sci Eng 13(2):375. https://doi.org/10.3390/jmse13020375

Linton CM (1988) Wave reflection by submerged bodies in water of finite depth. PhD thesis, University of Bristol, Bristol

Liu B, Park S (2023) CFD simulations of the effects of wave and current on power performance of a horizontal axis tidal stream turbine. J Mar Sci Eng 11(2):425. https://doi.org/10.3390/jmse11020425

Liu B, Park S (2024) Effect of wavelength on turbine performances and vortical wake flows for various submersion depths. J Mar Sci Eng 12(4):560. https://doi.org/10.3390/jmse12040560

Lloyd C, Allmark M, Ordonez-Sanchez S, Martinez R, Johnstone C, Germain G, Gaurier B, Mason-Jones A, O'Doherty T (2021) Validation of the dynamic load characteristics on a tidal stream turbine when subjected to wave and current interaction. Ocean Eng 222:108360. https://doi.org/10.1016/j.oceaneng.2020.108360

Lust EE, Luznik L, Flack KA, Walker JM, Van Benthem MC (2013) The influence of surface gravity waves on marine current turbine performance. Int J Mar Energy 3–4:27–40. https://doi.org/10.1016/j.ijome.2013.11.003

Lust EE, Flack KA, Luznik L (2020) Survey of the near wake of an axial-flow hydrokinetic turbine in the presence of waves. Renew Energy 146:2199–2209. https://doi.org/10.1016/j.renene.2019.08.067

Luznik L, Flack KA, Lust EE, Taylor K (2013) The effect of surface waves on the performance characteristics of a model tidal turbine. Renew Energy 58:108–114. https://doi.org/10.1016/j.renene.2013.02.022

McNaughton J, Zilic De Arcos F, Vogel CR, Willden RHJ (2025) Dynamic loading of two side-by-side tidal stream turbines in regular waves. J Fluids Struct 133:104259. https://doi.org/10.1016/j.jfluidstructs.2024.104259

Méhauté B (1976) An introduction to hydrodynamics and water waves. Springer, Berlin. https://doi.org/10.1007/978-3-642-85567-2

Messmer T, Hölling M, Peinke J (2024) Enhanced recovery caused by nonlinear dynamics in the wake of a floating offshore wind turbine. J Fluid Mech 984:A66. https://doi.org/10.1017/jfm.2024.175

Milne IA, Day AH, Sharma RN, Flay RGJ (2013a) Blade loads on tidal turbines in planar oscillatory flow. Ocean Eng 60:163–174. https://doi.org/10.1016/j.oceaneng.2012.12.027

Milne IA, Sharma RN, Flay RGJ, Bickerton S (2013b) Characteristics of the turbulence in the flow at a tidal stream power site. Philos Trans R Soc A Math Phys Eng Sci 371(1985):20120196. https://doi.org/10.1098/rsta.2012.0196

Molin B (2023) Offshore structure hydrodynamics. Cambridge ocean technology series, vol. 10. Cambridge University Press, Cambridge

Moreau M, Germain G, Maurice G, Richard A (2022) Sea states influence on the behaviour of a bottom mounted full-scale twin vertical axis tidal turbine. Ocean Eng 265:112582. https://doi.org/10.1016/j.oceaneng.2022.112582

Muller Y-A, Aubrun S, Masson C (2015) Determination of real-time predictors of the wind turbine wake meandering. Exp Fluids 56(3):53. https://doi.org/10.1007/s00348-015-1923-9

Mullings H, Stallard T (2022) Analysis of tidal turbine blade loading due to blade scale flow. J Fluids Struct 114:103698. https://doi.org/10.1016/j.jfluidstructs.2022.103698

Mycek P, Gaurier B, Germain G, Pinon G, Rivoalen E (2014) Experimental study of the turbulence intensity effects on marine current turbines behaviour. Part I: one single turbine. Renew Energy 66:729–746. https://doi.org/10.1016/j.renene.2013.12.036

Okulov VL, Sørensen JN (2010) Maximum efficiency of wind turbine rotors using Joukowsky and Betz approaches. J Fluid Mech 649:497–508. https://doi.org/10.1017/S0022112010000509

Oppenheim AV, Schafer RW (2014) Discrete-time signal processing, 3rd edn. Pearson New International edn. Always learning, vol. 1. Pearson, Harlow

Ouro P, Stoesser T (2019) Impact of environmental turbulence on the performance and loadings of a tidal stream turbine. Flow Turbul Combust 102(3):613–639. https://doi.org/10.1007/s10494-018-9975-6

Ouro P, Mullings H, Christou A, Draycott S, Stallard T (2024) Wake characteristics behind a tidal turbine with surface waves in turbulent flow analyzed with large-eddy simulation. Phys Rev Fluids 9(3):034608. https://doi.org/10.1103/PhysRevFluids.9.034608

Payne GS, Stallard T, Martinez R, Bruce T (2018) Variation of loads on a three-bladed horizontal axis tidal turbine with frequency and blade position. J Fluids Struct 83:156–170. https://doi.org/10.1016/j.jfluidstructs.2018.08.010

Peregrine DH (1976) Interaction of water waves and currents. In: Yih C-S (ed) Advances in applied mechanics, vol 16. Elsevier, Amsterdam, pp 9–117. https://doi.org/10.1016/S0065-2156(08)70087-5

Perez L, Cossu R, Grinham A, Penesis I (2022) Tidal turbine performance and loads for various hub heights and wave conditions using high-frequency field measurements and blade element momentum theory. Renew Energy 200:1548–1560. https://doi.org/10.1016/j.renene.2022.10.058

Posa A, Viola IM, Broglia R (2024) Influence of the tip speed ratio on the wake dynamics and recovery of axial-flow turbines. Phys Fluids 36(5):055109. https://doi.org/10.1063/5.0203285

Rey V, Guinot F, Le Boulluec M (2007) Wave-current interaction in finite water depth: effects on the kinematics. In: Actes des 11èmes Journées de l'Hydrodynamique. Comité des Journées de l'Hydrodynamique, Brest, France

Robins PE, Neill SP, Lewis MJ, Ward SL (2015) Characterising the spatial and temporal variability of the tidal-stream energy resource over the northwest European shelf seas. Appl Energy 147:510–522. https://doi.org/10.1016/j.apenergy.2015.03.045

Roy AG, Buffin-Blanger T, Lamarre H, Kirkbride AD (2004) Size, shape and dynamics of large-scale turbulent flow structures in a gravel-bed river. J Fluid Mech 500:1–27. https://doi.org/10.1017/S0022112003006396

Scarlett GT, Sellar B, Van Den Bremer T, Viola IM (2019) Unsteady hydrodynamics of a full-scale tidal turbine operating in large wave conditions. Renew Energy 143:199–213. https://doi.org/10.1016/j.renene.2019.04.123

Segalini A, Alfredsson PH (2013) A simplified vortex model of propeller and wind-turbine wakes. J Fluid Mech 725:91–116. https://doi.org/10.1017/jfm.2013.182

Slama M, Pinon G, Hadi CE, Togneri M, Gaurier B, Germain G, Facq J-V, Nuño J, Mansilla P, Nicolas E, Marcille J, Pacheco A (2021) Turbine design dependency to turbulence: an experimental study of three scaled tidal turbines. Ocean Eng 234:109035. https://doi.org/10.1016/j.oceaneng.2021.109035

Smyth ASM, Zilic De Arcos F, Young AM (2025) Modelling unsteady hydrodynamic gust loading on tidal turbine blades. J Fluids Struct 137:104381. https://doi.org/10.1016/j.jfluidstructs.2025.104381

Tatum SC, Frost CH, Allmark M, O'Doherty DM, Mason-Jones A, Prickett PW, Grosvenor RI, Byrne CB, O'Doherty T (2016) Wave-current interaction effects on tidal stream turbine performance and loading characteristics. Int J Mar Energy 14:161–179. https://doi.org/10.1016/j.ijome.2015.09.002

Tedds SC, Owen I, Poole RJ (2014) Near-wake characteristics of a model horizontal axis tidal stream turbine. Renew Energy 63:222–235. https://doi.org/10.1016/j.renene.2013.09.011

Tennekes H, Lumley JL (1972) A first course in turbulence. The MIT Press, Cambridge. https://doi.org/10.7551/mitpress/3014.001.0001

Thomson J, Polagye B, Durgesh V, Richmond MC (2012) Measurements of turbulence at two tidal energy sites in Puget Sound, WA. IEEE J Oceanic Eng 37(3):363–374. https://doi.org/10.1109/JOE.2012.2191656

Tian W, Ni X, Mao Z, Zhang T (2020) Influence of surface waves on the hydrodynamic performance of a horizontal axis ocean current turbine. Renew Energy 158:37–48. https://doi.org/10.1016/j.renene.2020.04.127

Tisserand É, Pautex J-F, Schweitzer P (2009) Analyse et Traitement des Signaux: Méthodes et Applications Au Son et à L'image Cours et Exercices Corrigés, 2e éd edn. Sciences sup, vol. 1. Dunod, Paris

Tobin N, Zhu H, Chamorro LP (2015) Spectral behaviour of the turbulence-driven power fluctuations of wind turbines. J Turbul 16(9):832–846. https://doi.org/10.1080/14685248.2015.1031242

Toloui M, Chamorro LP, Hong J (2015) Detection of tip-vortex signatures behind a 2.5 MW wind turbine. J Wind Eng Ind Aerodyn 143:105–112. https://doi.org/10.1016/j.jweia.2015.05.001

Trujillo J-J, Bingöl F, Larsen GC, Mann J, Kühn M (2011) Light detection and ranging measurements of wake dynamics part II: two-dimensional scanning. Wind Energy 14(1):61–75. https://doi.org/10.1002/we.402

Vahidi D, Porté-Agel F (2024) Influence of incoming turbulent scales on the wind turbine wake: a large-eddy simulation study. Phys Fluids 36(9):095177. https://doi.org/10.1063/5.0222372

Watanabe S, Kamra MM, Hu C (2023) An experimental study of surface wave effects on two interacting tidal turbines. J Mar Sci Technol 28(2):387–398. https://doi.org/10.1007/s00773-023-00929-6

Wei NJ, El Makdah A, Hu J, Kaiser F, Rival DE, Dabiri JO (2024) Wake dynamics of wind turbines in unsteady streamwise flow conditions. J Fluid Mech 1000:A66. https://doi.org/10.1017/jfm.2024.999

Welch P (1967) The use of fast Fourier transform for the estimation of power spectra: a method based on time averaging over short, modified periodograms. IEEE Trans Audio Electroacoust 15(2):70–73. https://doi.org/10.1109/TAU.1967.1161901

Whelan JI, Graham JMR, Peiro J (2009) Inertia effects on horizontal axis tidal-stream turbines. In: Proceedings of the 8th European wave and tidal energy conference (EWTEC). EWTEC Secretariat, Uppsala, Sweden

Wood DH, Boersma J (2001) On the motion of multiple helical vortices. J Fluid Mech 447:149–171. https://doi.org/10.1017/S002211200100578X

Zilic De Arcos F, McNaughton J, Vogel C, Pinon G (2023) A study on tidal rotors under the combined effects of currents and waves using actuator-line CFD simulations. In: Proceedings of the 15th European wave and tidal energy conference (EWTEC), vol 15. EWTEC Secretariat, Bilbao, Spain. https://doi.org/10.36688/ewtec-2023-367